Advanced Casting Research Center (ACRC) Consortium Meeting

December 4-5, 2001

Report 01-#2

Metal Processing Institute
WPI, Worcester, MA 01609 USA
www.wpi.edu/+mpi

TABLE OF CONTENTS

A. Modeling of Rheology in Semi-Solid Alloys

MODELING OF RHEOLOGY IN SEMISOLID ALLOYS

Report No. PR–01#2

Research Team:	Philippe LeMenn		
	Andreas Alexandrou	+357-2-892256	andalexa@ucy.ac.cy
Focus Group:	Craig Bergsma		Northwest Aluminum
	Tom Caldwell		Madison-Kipp Corp.
	Ray Donahue		Mercury Marine
	Eric Erike		TRW
	John Jorstad		JLJ Technologies
	Steve Midson		Formcast
	Mike Thieman		THT Presses
	Per Arne Tondel		Elkem Aluminum
	Steve Udvardy		NADCA
	Jim Van Wert		Amcast
	Josef Woehrer		Salzburger Aluminum

PROJECT STATEMENT

Objectives

(a) Develop a general mathematical and computational model that can describe the flow of semisolid materials.

(b) Study various flows through modeling and simulation in order to validate the models and to study the flow behavior at the level allowed by the mathematical models. Obtain insight into the bulk flow of semisolid materials and help identify the influence of various flow parameters on the final product.

Strategy

Developed a general phenomenological mathematical model that describes the flow of viscoplastic materials with shear and time dependent properties and used actual experimental data to fit the model parameters.

ACHIEVEMENTS TO DATE

The following tasks were completed:

- Development of mathematical and computational models
- Study of basic flow geometries and development of processing maps
- Document the stability for semisolid material flow into a simple cavity

CHANGES IN PROJECT STATEMENT

None

WORK PLANNED FOR THE NEXT QUARTER

Determine the material constants through "reversed engineering". This includes modeling of the compression experiments performed by Pan and Apelian to establish the constants in the constitutive relations

PROJECT SCHEDULE

Task	November	December	January	February	March	April
Mathematical Model	xxxxxxxxx	xxxxx				
Computational code	xxxx	xxxxxxxxx	xxxxxxxx			
Numerical Simulations			xxxxxx	xxxxxxxx	xxxxxxxx	xxxxxxxx
Report				xxxxxxxx	xxxxxxxx	xxxxxxxx

APPENDIX

A.N. Alexandrou, P. LeMenn, D. Apelian, "On the Reliability of the Semisolid Process," Metallurgical Transactions (to be submitted).

Appendix A

Flow Instabilities in Herschel-Bulkley Fluids

Andreas N. *Alexandrou*[a,1], Philippe Le *Menn*[a],
Vladimir Entov[b] and George C. Georgiou[c]

[a] *Semisolid Metal Processing Lab, MPI, Worcester Polytechnic Institute*
Worcester, MA 01609, USA

[b] *Institute for Problems in Mechanics of the Russian Academy of Science*
pr. Vernadskogo, 101, 117526 Moscow, Russia

[c] *Department of Mathematics, University of Cyprus*
CY 1618, Nicosia, Cyprus

Abstract

In this paper we investigate the interaction of a two-dimensional jet of a Herchel-Bulkley fluid with a vertical surface at a distance L from the die exit. This problem also simulates the early stages of filling of a two-dimensional cavity. The main purpose of this work is to study numerically flow instabilities for this flow arrangement. Results are obtained for a range of Reynolds and Bingham numbers, and we establish the effects of these dimensionless numbers on both the filling, and the stability of the jet.

1 Introduction

Materials that exhibit no deformation below a finite applied shear stress (τ_o) are known as Bingham plastics [1]. Examples of such materials include paint, slurries, aqueous foams, pharmaceutical products, pastes, polymeric solutions, paper pulp, food substances like margarine, mayonnaise and ketchup [2], colloidal suspensions [3], plastic propellant doughs [4], drilling fluids [5], and semisolid materials [6].

The motivation of the present work is our interest in the processing of semisolid slurries. These are two-phase slurries whose behavior can be represented using a Herschel-Bulkley fluid model. In processing of such slurries filling patterns are often irregular and unpredictable, pointing to the existence of possible instabilities. Here, we investigate the "toothpaste" behavior which is a typical flow instability observed in semisolid slurry processing. Figure 1 shows an experimental observation of such an instability: as shown, even though the part is symmetric, the left arm develops a wave-like pattern after the jet hits the closed-end of the cavity. A similar jet profile is also shown in Fig. 2. The name "toothpaste" comes from the similarity between this instability and the toothpaste behavior when forced out of its tube. From a practical point of view such instabilities are undesirable and can lead to non-uniformities in the parts being made. Investigations by Midson et al. [7, 8] provide further evidence of these instabilities, and demonstrate experimentally that slow filling yields the "best" die filling behavior, with mostly laminar flow, and the least amount of material folding. In general, these instabilities originate at the point where the filling front in the form of a jet meets the wall of the cavity. Therefore, the jet-vertical wall arrangement chosen here represents well the early stages of filling of a 2-D cavity. To our knowledge no similar investigation has been reported in the literature.

Several rheological equations and yield criteria have been proposed [9, 10, 11] to describe the stress-deformation behavior of materials exhibiting a yield stress. The most commonly used model is the Bingham model [1, 12, 13], which in tensorial form is expressed as:

$$\underline{\underline{\dot{\gamma}}} = 0 \quad \text{for} \quad \tau \leq \tau_o, \tag{1}$$

$$\underline{\underline{\tau}} = \left(\eta + \frac{\tau_o}{\dot{\gamma}}\right)\underline{\underline{\dot{\gamma}}} \quad \text{for} \quad \tau > \tau_o, \tag{2}$$

where $\underline{\underline{\dot{\gamma}}} = \left(\nabla \mathbf{u} + \nabla \mathbf{u}^{\mathbf{T}}\right)$ represents the rate of strain tensor, $\underline{\underline{\tau}}$ the extra stress tensor, τ_o the yield stress and η the viscosity of the deformed material. τ and $\dot{\gamma}$ are respectively the second invariants of the extra stress and rate of strain tensors, defined as:

$$\tau = \left[\frac{1}{2}\tau_{ij}\tau_{jk}\right]^{1/2} \quad \text{and} \quad \dot{\gamma} = \left[\frac{1}{2}\dot{\gamma}_{ij}\dot{\gamma}_{jk}\right]^{1/2}. \tag{3}$$

The rheological behavior of a Bingham fluid is characterized by two different flow regimes: if $\tau \leq \tau_\circ$ the material behaves as a rigid solid. If $\tau \geq \tau_\circ$ it flows with the apparent viscosity $\eta_{app} = \eta + \frac{\tau_o}{\dot{\gamma}}$.

The Herschel-Bulkley model is a generalization of the Bingham model that takes into account changes in the effective viscosity with the applied shear rate. The Herschel-Bulkley model assumes that the effective viscosity upon deformation follows a power-law behavior:

$$\eta = \kappa \dot{\gamma}^{n-1}, \tag{4}$$

where n and κ are the power-law and consistency indices, respectively. The fluid behavior is shear-thickening for $n > 1$, and shear-thinning for $n < 1$. For $n = 1$, the Herschel-Bulkley model reduces to the Bingham model with the consistency index equivalent to the viscosity.

The two distinct regions (yielded ($\tau > \tau_o$) and unyielded ($\tau < \tau_o$)) of the fluid are separated by the "yield surface" defined as the surface where the local stress is equal to the yield stress. In numerical modeling, in addition to the non-linearities in the governing equations, an inherent difficulty is the discontinuity in the constitutive relation. Due to the presence of $\dot{\gamma}$ in the denominator of Eq. (2), the apparent viscosity becomes unbounded at vanishing shear rates. Also, while calculating the velocity field the shape and location of the yield surface are unknown. Although this does not constitute any limitation in analytic solutions in simple cases such as flow in tubes [14], it introduces significant difficulties in more complicated problems that are only amenable to numerical analysis. To overcome these issues, several modified versions of Eqs. (1) and (2) have been proposed [15, 16, 17, 18]. Keunings [19] reviews current developments in the field of computational rheology applied to the prediction of the flow of polymeric liquids, i.e., highly non-Newtonian materials, in complex geometries. Many of the reviewed papers are representative of current trends in the field of numerical modeling of Herschel-Bulkley fluids.

For numerical modeling purposes, a common approach is to approximate the rheological behavior of the fluid to be valid uniformly at all levels of stress. Papanastasiou [15] introduced a regularization parameter m that controls the

exponential rise in the stress at low rates of strain:

$$\underline{\underline{\tau}} = \left[\eta + \tau_{\circ} \frac{1 - exp\,(-m\dot{\gamma})}{\dot{\gamma}}\right] \underline{\underline{\dot{\gamma}}}. \tag{5}$$

The parameter m has dimensions of time. This constitutive relation is expressed in terms of three independent material parameters, τ_o, κ, and n, which are determined from experimental data. The Herschel-Bulkley behavior is approximated for relatively large m values. According to Eq. (5) for $\dot{\gamma} \approx 0$ the apparent viscosity is finite, given by $\eta_{app} \approx (\eta + m\tau_o)$. The constitutive relation is then expressed as $\underline{\underline{\tau}} \approx (\eta + m\tau_o)\underline{\underline{\dot{\gamma}}}$. Papanastasiou [15] validated this model on several simple flows such as one-dimensional channel flow, two-dimensional boundary layer flow and extrusion flow. The accuracy and effectiveness of this model in representing Herschel-Bulkley fluids has also been demonstrated by Elwood et al. [20], Mitsoulis and Abdali [21], Tsamopoulos et al. [22], Blackery and Mitsoulis [23] and Burgos et al. [18, 24].

Experimental data reported by Ellwood et al. [20], Keentok et al. [25] and Dzuy et al. [26] actually demonstrate that a continuous model provides a better approximation to experimental data than the ideal model. Therefore, it is postulated that the ideal Bingham model may be only a theoretical idealization. Recent investigations by Blackery and Mitsoulis [23], Beaulne and Mitsoulis [27], Papanastasiou and Boudouvis [28] concentrate on problems that involve Bingham and Herschel-Bulkley fluids. In these studies the material was also modeled using Papanastasiou's regularized constitutive equation.

In a recent study, Alexandrou et al. [29] investigated filling of a 2-D cavity by Bingham fluids. They examined the relative importance of inertial, viscous and yield stress effects on the filling profiles. They identified five characteristic filling patterns: "mound," "disk," "shell," "bubble" and a "transition" between that of "mound" and "bubble" patterns. A summary of these different flow behaviors is shown in Fig. 3. These characteristic flow patterns highlight the important role of the finite yield stress in Bingham fluids. Experimental studies confirmed the existence of the numerically obtained patterns; the "mound," "disk," and "shell" patterns have been observed by Paradies and Rappaz [30] in semisolid processing. Recent experimental results by Koke et al. [31] also confirmed these patterns by using

model substances such as chocolate cream, calcium-carbonate/oil suspension, tomato paste, ultrasonic gel and Newtonian silicone oil.

The main objective of the present work is to investigate the stability of a jet of a Herschel-Bulkley fluid emanating from a die and impinging on a vertical wall. As discussed earlier, this flow arrangement simulates also the early stages of filling of a 2-D cavity. Since the results obtained by Alexandrou et al. constitute the equilibrium states for the problem considered here, for the purpose of the present study we also simulated the cases considered in [29].

2 Mathematical and Computational Model

2.1 Governing Equations

The schematic of the problem considered here is shown in Fig. 4. The 2-D geometry is characterized by the inlet section (length l and height H). The material is injected in the die from the left side and hits the vertical solid surface at a distance L away. The flow was modeled using the conservation of mass and momentum for an incompressible fluid:

$$\nabla \cdot \mathbf{u} = 0, \tag{6}$$

$$\rho \left[\frac{\partial \mathbf{u}}{\partial t} + \mathbf{u} \cdot \nabla \mathbf{u} \right] = \nabla \cdot \underline{\underline{\sigma}}, \tag{7}$$

where $\mathbf{u}$ is the velocity vector, ρ the density of the fluid, and $\underline{\underline{\sigma}}$ the total stress tensor, which is given by

$$\underline{\underline{\sigma}} = -P\underline{\underline{I}} + \underline{\underline{\tau}}.$$

Here P represents the total pressure, $\underline{\underline{I}}$ the unit tensor, and $\underline{\underline{\tau}}$ the viscous stress tensor. The body force per unit volume due to gravity was neglected in this study.

2.2 Non-Dimensionalization

The set of governing equations (Eqs. (6) and (7)) were non-dimensionalized using:

$$x_i^* = \frac{x_i}{H};\ \ t^* = \frac{t}{H/U_o};\ \ \mathbf{u}^* = \frac{\mathbf{u}}{U_o};\ \ P^* = \frac{P}{\tau_o};\ \ \underline{\underline{\tau}}^* = \frac{1}{\tau_o}\underline{\underline{\tau}};\ \ \underline{\underline{\sigma}}^* = \frac{1}{\tau_o}\underline{\underline{\sigma}}, \tag{8}$$

where H is taken as the inlet height and U_o the average inlet velocity. Due to the non-dimensionalization the imposed volumetric flow rate is $Q^* = 1$.

2.3 Dimensionless Equations

Using the dimensionless groups introduced in Eq. (8) we can rewrite the governing equations in a dimensionless form:

$$\nabla \cdot \mathbf{u}^* = 0, \tag{9}$$

$$Re\left[\frac{\partial \mathbf{u}^*}{\partial t^*} + \mathbf{u}^* \cdot \nabla \mathbf{u}^*\right] = Bi \nabla \cdot \underline{\underline{\sigma}}^*. \tag{10}$$

Here,

$$\underline{\underline{\sigma}}^* = -P^* \underline{\underline{I}} + \underline{\underline{\tau}}^*,$$

is the total non-dimensional stress tensor. According to Eqs. (9) and (10) the fluid behavior depends on two dimensionless parameters, the Reynolds (Re) and Bingham (Bi) numbers, defined respectively as:

$$Re = \frac{\rho U_o H}{\eta_{eff}} \quad \text{and} \quad Bi = \frac{\tau_o H}{\eta_{eff} U_o}. \tag{11}$$

The effective viscosity η_{eff} is obtained from the one-dimensional analog of the constitutive equation (Eq. (5)):

$$\tau = \tau_o + \kappa \dot{\gamma}^n = \tau_o + \kappa \mid \dot{\gamma} \mid^{n-1} \dot{\gamma}, \tag{12}$$

where $\dot{\gamma}$ is the shear rate, and $\eta_{eff} = \kappa \mid \dot{\gamma} \mid^{n-1}$ is the effective viscosity.

Therefore, the Reynolds and Bingham numbers are generalized as:

$$Re = \frac{\rho U_o^{(2-n)} H^n}{\kappa} \quad \text{and} \quad Bi = \frac{\tau_o H^n}{\kappa U_o^n}. \tag{13}$$

The Herschel-Bulkley constitutive relation, Eq. (5), can thus be rewritten in a dimensionless form:

$$\underline{\underline{\tau}}^* = \left[\frac{1}{Bi}\dot{\gamma}^{*(n-1)} + \frac{[1 - exp\,(-m^*\dot{\gamma}^*)]}{\dot{\gamma}^*}\right]\underline{\underline{\dot{\gamma}}}^*, \tag{14}$$

where $\underline{\underline{\dot{\gamma}}}^*$ is the dimensionless rate of strain tensor, $\dot{\gamma}^*$ its second invariant, and m^* the dimensionless growth exponent, which are respectively defined as

$$\underline{\underline{\dot{\gamma}}}^* = \frac{1}{U_o/H}\underline{\underline{\dot{\gamma}}}; \quad \dot{\gamma}^* = \frac{\dot{\gamma}}{(U_o/H)^2}; \quad m^* = \frac{mU_o}{H}. \tag{15}$$

Equation (14) has only two independent material parameters (Bi and n), whereas Eq. (5) had three (κ, τ_o, and n). Hereafter, for convenience, the asterisk ($*$) is dropped from the non-dimensional variables and all physical quantities mentioned are implicitly dimensionless.

The flow is established by applying a fixed dimensionless volumetric flow rate (i.e., Q=1) at the inlet with a parabolic velocity profile imposed at the entrance plane of the inlet. The inlet length is fixed at a sufficient distance l so that the flow becomes fully developed prior to reaching the exit of the die. In this study the non-dimensional length of the inlet was fixed at $l = 5$ which was found to be sufficient to ensure fully developed flow in the die. Along the die walls the velocity was set to zero. The same no-slip condition was imposed at the end-wall.

As mentioned earlier, different lengths L were used in order to study the influence of this geometrical parameter on the stability of the jet. The simulation is initialized when the jet emanating from the inlet section reaches the end-wall. The initial jet profile is taken from the steady state results, and corresponds to a column of fluid hitting the end-wall at velocities $u \approx 1$, $v \approx 0$.

3 Method of Solution

The governing equations and constitutive relation were discretized using the classical mixed-Galerkin finite element method with nine-node rectangular elements. The resulting non-linear system of equations was linearized using a Newton-Raphson iteration procedure. For converged results in the

Newton-Raphson iterative scheme, usually three to four iterations were necessary at each time step.

A detailed presentation of the mixed-Galerkin finite element discretization for the extrusion problem can be found in [20, 32, 33]. The nonlinear system of equations resulting from this analysis is then solved by Newton-Raphson iteration. The spatial discretization reduces the set of equations to a system of ordinary differential equations:

$$\mathbf{M} \cdot \frac{\partial \mathbf{q}}{\partial t} + \mathbf{R}(\mathbf{q}) = 0, \tag{16}$$

where $\mathbf{q} = [u_1(y,z,t), v_1(y,z,t), ..., h_{N_h}(z,t)]$ is the vector of all the time-dependent nodal unknowns, $\mathbf{R}$ is the column vector of the time-dependent Galerkin residuals. The time derivatives are discretized by a standard backward difference scheme,

$$\mathbf{M} \cdot \frac{\partial \mathbf{q}}{\partial t} \equiv \mathbf{M} \cdot \left[\frac{\mathbf{q}^{n+1} - \mathbf{q}^n}{\Delta t} \right] = \mathbf{R}(\mathbf{q}^{n+1}). \tag{17}$$

Thus all the nodal unknowns of the velocity components and pressure are evaluated simultaneously. The free surface is calculated automatically by properly assigning the velocity of the nodes along the free surface to reflect the fact that the free surface is a material surface.

Equation (17) is then solved at each time step by Newton-Raphson iteration for $\mathbf{u}$, P, and h. The set of linear equations is repeatedly solved by a frontal technique [34, 35, 36] developed by Hood [37]. The tessellation is updated at every iteration with the newly found free surface. The initial conditions are those of a jet from its steady state. The initial velocity and pressure fields are determined from the steady-state counterpart of the problem at the initial configuration.

4 Results

In this work, we concentrate on a problem equivalent to that of die filling, i.e., the interaction of a Herschel-Bulkley fluid jet and a vertical surface at a distance L from the die exit and we study the interplay between inertia, viscous drag and yield stress, or as expressed in terms of force per

unit depth, $F_i \equiv \rho U_o^2 H$, $F_v \equiv \eta U_o$, and $F_{\tau_o} \equiv \tau_o H$ respectively (Fig. 5). Non-dimensional analysis shows that the flow depends on two dimensionless parameters: the Reynolds (Re) and Bingham (Bi) numbers. The Reynolds number represents the F_i/F_v ratio, while the Bingham number indicates the F_{τ_o}/F_v ratio. A third choice is the Saint-Venant number which indicates the importance of the yield stress effects relative to inertia forces (F_{τ_o}/F_I) and which is defined as:

$$Sv = \frac{Bi}{Re} = \frac{\tau_o}{\rho U_o^2}. \tag{18}$$

Obviously, only two of these three parameters are independent. The appropriate choice of parameters depends on the flow regime being analyzed. The effects of Re and Bi are investigated using the two-dimensional geometry shown in Fig. 4, with the finite-element mesh shown in Fig. 6.

The parameter m in the regularized model was set to a value of $m = 1000$, which was found to be high enough to insure results independent of m. The reported results are also mesh and time-step independent. A more pertinent study of the effect of m on the accuracy of the results can be found in [18, 24]. The power-law index n was set to a value of $n = 1$ as in [29].

Figure 7 shows the results for conditions similar to those in [29]. The five typical flow behaviors reported in [29] have been reproduced here as well, providing thus further evidence on the existence of these patterns. Table 1 summarizes the flow parameters for the flow patterns shown in the aforementioned figure.

Re	Bi	$FlowPattern$
500	10	Shell
6	0.1	Disk
0.5	0.1	Mound
1	3	Bubble
10	1.7	Transition

Table 1: Flow parameters used for the displayed jet behaviors ($L = 10$ geometry).

The figure also shows the topography of the yielded and unyielded regions. As shown in the figure, only the "bubble" and "transition" patterns

exhibit significant unyielded zones. Therefore the first three patterns behave in a manner consistent with a viscous fluid. The "bubble" and "transition" patterns, though, are expected to be influenced by the yield stress effects. As we will demonstrate below, flow instabilities are primarily connected to these two patterns.

The following results examine the interaction of the Herschel-Bulkley jet with a vertical wall as a function of rheological and geometrical parameters. Numerical simulations of flows that in real life are unstable may fail to predict flow instabilities. This is due to the almost perfect symmetry of numerical results, and due to the fact that numerical errors take a long time to grow to a magnitude that can trigger instabilities. Therefore, it is customary to introduce an artificial disturbance to disrupt the symmetry of the flow. This artificial instability is typically very small, and it is applied for a short duration. Here, a small disturbance is introduced in the flow by imposing an asymmetric velocity profile at the inlet for a short time Δt, beginning at the moment the jet reaches the vertical wall (defined as $t = 0$ in the following). For $t > \Delta t$, the inlet velocity was kept constant and symmetric. In both the symmetric and asymmetric cases the volumetric flow rate was kept constant. The flow field and the jet stability are found to be independent of the magnitude and the duration of the asymmetry.

The finite-element mesh used in the simulations is refined around zones that are sensitive to flow singularities and where gradients are large (die exit and end-wall). The case $n \neq 1$ is considered at the end of the present study. The unsteady simulation is initiated at the time where the jet hits the vertical wall ($t = 0$). The initial conditions were taken from the steady solution of the problem for the configuration when the jet is about to touch the wall. The geometry used here includes an inlet section ($H = 1$, $l = 5$), and a vertical wall at a distance L from the exit of the die. Results are also shown for variable values of L. Typical jet-wall interactions obtained numerically are shown in Figs. 8 and 9, as sequences of 'snapshots' of the jet profile, where t is the non-dimensional time.

Figure 8 shows the jet behavior for the $L = 10$ geometry at a low Reynolds number ($Re = 1$) and at a moderate Bingham number ($Bi = 3$). For a symmetric velocity profile at the inlet (i.e., no disturbance), these conditions lead to a "bubble" pattern. Here, when the jet emanating from the inlet section reaches the vertical wall, it grows as a "bubble" up to a dimensionless

time $t \approx 7$. When the disturbance is introduced from the start of the flow ($t = 0$) until $t = \Delta t = 1.5$, it triggers an instability which forces the jet to bend, very much like the buckling of a slender solid column. This flow behavior is very similar to what is observed experimentally and described as the "toothpaste" effect. For the discussion that follows such behavior is labeled as "unstable".

The flow shown in Fig. 9 is obtained for $Re = 5$ and $Bi = 1$. For both symmetric and asymmetric flow conditions the jet grows in a manner consistent with a "transition" pattern. Therefore, the initial disturbance has no impact on the stability of the jet, and no noticeable difference can be observed between the symmetric and asymmetric cases. In the discussion below this flow behavior is labeled as "stable".

Figure 10 shows a complete map of the jet profiles as a function of the Reynolds and Bingham numbers for the range $0.5 \leq Re \leq 50$, $0 < Bi \leq 40$. This map clearly shows the regions where "stable" and "unstable" patterns occur. The estimated boundary between these two zones has been sketched in in order to demarcate the range of Re and Bi which they correspond to. On this map, the symbols ▲, ●, ■, ▼ represent respectively the "mound," "disk," "bubble" and "transition" patterns. The hollow symbols (□, and ▽) represent the cases discussed in detail (Figs. 8 and 9). As speculated, while "bubble" pattern leads to unstable jet behavior, "shell," "disk" and "mound" patterns remain stable and most of the "transition" cases lead to stable jet profiles. The "bubble" pattern is very sensitive to flow instabilities, that prevent this pattern to develop. These numerical results explain why experimental observations of the "bubble" pattern are not as common as the other patterns. It is clear from the results that the instabilities are indeed the result of the finite yield stress and the way yielded and unyielded regions interact with each other.

As mentioned earlier, it is possible to express the results in terms of the Saint-Venant number as shown in Fig. 11. In the map, the squares (■) represent stable configurations and the upward pointing triangles (▲) correspond to unstable behaviors. The hollow markers (□ and △) correspond to the cases shown in Figs. 8 and 9. The advantage of considering the Saint-Venant number is that it is independent of the characteristic length scale parameter H, and is expressed in terms of fluid properties and kinematics of the flow.

So far the length L was kept constant. However, the stability characteristics depend also on the length of the die L. The effect of the distance between the die exit and the vertical wall was established by using three different lengths $L = 10$, 15 and 20. Figure 12 highlights this effect on the stability of the jet for given rheological parameters ($Re = 1$, $Bi = 0.7$). The jet behavior is either stable and symmetric (Fig. 12(a), $L = 10$) or unstable and toothpaste-like (Fig. 12(b), $L = 15$, and (c), $L = 20$). This demonstrates that the longer the die, the more likely it is to observe the toothpaste instability. Figure 13 summarizes this behavior in a manner similar to Fig. 10 for $L = 15$ and $L = 20$. The map shows the estimated boundaries between stable and unstable jet behavior for the three lengths studied. The solid line represents the $L = 10$ case while the dashed line and the dashdotted line stand for the $L = 15$ and $L = 20$ cases, respectively. From that figure, the overall jet stability is confirmed: the longer L, the more likely it is to observe toothpaste-like instabilities.

The results shown are for Bingham fluids ($n = 1$). However, once the yield stress is exceeded, Herschel-Bulkley fluids flow either in a shear-thinning or shear-thickening manner. The effect of the power-law exponent was studied for two cases: one corresponding to a shear-thinning fluid ($n = 0.5$) and another to a shear-thickening fluid ($n = 1.5$). For both cases the length was set to $L = 15$. Figure 14 shows the overall stability behavior as a function of n. Again, limiting lines separate stable and unstable behaviors. The solid line represents the $n = 1$ case while the dashed line and the dashdotted line stand for the $n = 0.5$ and $n = 1.5$ cases, respectively. A shift between the three limiting lines can be observed: the smaller the power-law index, the more unstable the flow is. In other words, a shear-thinning behavior is more sensitive to instabilities than a shear-thickening one. It appears also that the power-law index becomes less important (actually it is not important at all) for large values of Bi. This is due to the fact that for large Bi the flow behaves more like a solid as very little of the fluid deforms.

5 Conclusions

The numerical simulations presented in this study verify the importance of the finite yield stress in Herschel-Bulkley flows. The results confirm the

existence of five characteristic flow patterns ("shell," "disk," "mound," "bubble" and "transition") that have been observed both experimentally and numerically. By controlling flow parameters, one may be able to a priori fix jet behavior to lead to desirable quality and properties of the final parts.

In actual Herschel-Bulkley flows, the injection process is very sensitive to flow instabilities which may lead to irregular and unpredictable filling patterns. This undesired behavior is likely to happen at distinct combinations of flow parameters. Stability maps of the injection process have been drawn as a function of these parameters. It was concluded that the most unstable pattern is that of "bubble" and to a lesser degree that of the "transition" pattern, primarily due to the effects of the yield stress.

Acknoledgments: Partial support for this study was provided by Aluminium Pechiney, France.

References

[1] Bingham E. C. *Fluidity and Plasticity.* McGraw-Hill, 1922.

[2] Vradis G. C., and Ötűgen M. V. The axisymmetric sudden expansion flow of a non-Newtonian viscoplastic fluid. *Journal of Fluids Engineering*, 119:193–200, 1997.

[3] Covey G. H. and Stanmore B. R. Use of parallel-plate plastometer for the characterization of viscous fluids with yield stress. *Journal of Non-Newtonian Fluid Mechanics*, 8:249, 1981.

[4] Carter R. E. and Warren R. C. Extrusion stresses, die swell, and viscous heating effects in double-phase propellants. *Journal of Rheology*, 31:151–173, 1987.

[5] Azouz I., Shirazi S. A., Pilehvari A., and Azar J. J. Numerical simulation of laminar flows of yield-power-law fluids in conduits of arbitrary cross-section. *Journal of Fluids Engineering*, 115:710–716, 1993.

[6] Ahmed A. and Alexandrou A. N. Processing of semisolid materials using a shear-thickening Bingham fluid model. In *Proceeding of the*

1994, ASME Fluids Engineering Division Summer Meeting, FED-Vol. 179, pages 83–87, New York, 1994.

[7] Midson S. P., Minkler R. B., and Brucher H. B. Gating of semisolid aluminum castings. In *6th International Conference on Semisolid Processing of Alloys and Composites, Conference Proceedings*, pages 67–71, Turin, Italy, 27-29 September 2000.

[8] Midson S. P., Thornhill L. E., and Young K. P. Influence of key process parameters on the quality of semisolid metal cast aluminum components. In *5th International Conference on Semisolid Processing of Alloys and Composites, Conference Proceedings*, pages 181–188, Golden, CO, 23-25 June 1998.

[9] Fredrickson A. G. *Principles and applications of rheology.* Prentice Hall, Englewood Cliffs, NJ, 1964.

[10] Argon A. S. *Constitutive equations in plasticity.* MIT Press, Cambridge, MA, 1975.

[11] Malvern L. E. *An introduction to the mechanics of the continuous medium.* Prentice Hall, Englewood, NJ, 1969.

[12] Oldroyd J. G. A rational formulation of the equations of plastic flow for a Bingham solid. *Proceedings of the Cambridge Philosophical Society*, 43:100–105, 1947.

[13] Bird R. B., Dai G. C., and Yarusso B. J. The rheology and flow of viscoplastic materials. *Rev. Chemical Engineering*, 1:1–70, 1983.

[14] Bird R. B. and Armstrong R. C. *Dynamics of polymeric liquids.* John Wiley and Sons, New-York, NY, 1977.

[15] Papanastasiou T. C. Flows of materials with yield. *Journal of Rheology*, 31:385–404, 1987.

[16] Bercovier M. and Engelman M. A finite element method for incompressible non-Newtonian flows. *Journal of Computational Physics*, 36:313–326, 1980.

[17] O'Donovan E. J. and Tanner, R. I. Numerical study of the Bingham squeeze film problem. *Journal of Non-Newtonian Fluid Mechanics*, 15:75–83, 1984.

[18] Burgos G. R., Alexandrou A. N., and Entov V. On the determination of yield surfaces in Herschel-Bulkley fluids. *Journal of Rheology*, 43:463–483, 1999.

[19] Keunings B. Advances in the computer modeling of the flow of polymeric liquids. *accepted for publication in Computational Fluid Dynamics Journal*, ??:??, 1999.

[20] Ellwood K. R. J., Georgiou G. C., Papanastasiou T. C., and Wilkes J. O. Laminar jets of Bingham-plastic liquids. *Journal of Rheology*, 34:787–811, 1990.

[21] Mitsoulis E., Abdali S. S., and Markatos N. C. Flow simulation of Herschel-Bulkley fluids through extrusion dies. *The Canadian Journal of Chemical Engineering*, 71:147–160, 1993.

[22] Tsamopoulos J. A., Chen M. F., and Borkar A. V. On the spin coating of viscoplastic fluids. *Rheologica Acta*, 35:597–615, 1996.

[23] Blackery J. and Mitsoulis E. Creeping motion of a sphere in tubes filled with a Bingham plastic material. *Journal of Non-Newtonian Fluid Mechanics*, 70:59–77, 1997.

[24] Burgos G. R. and Alexandrou A. N. Flow development of Herschel-Bulkley fluids in a sudden 3-D square expansion. *Journal of Rheology*, 43:485–498, 1999.

[25] Keentok M., Milthorpe J. F., and O'Donovan E. On the shearing zone around rotating vanes in plastic liquids: theory and experiment. *Journal of Non-Newtonian Fluid Mechanics*, 17:23, 1985.

[26] Dzuy N. Q. and Boger D. V. Direct yield stress measurement with the vane method. *Journal of Rheology*, 29:334, 1985.

[27] Beaulne M. and Mitsoulis E. Creeping motion of a sphere in tubes filled with Herschel-Bulkley fluids. *Journal of Non-Newtonian Fluid Mechanics*, 72:55–71, 1997.

[28] Papanastasiou T. C. and Boudouvis A. G. Flows of viscoplastic materials: models and computations. *Computers and Structures*, 64:677–694, 1997.

[29] Alexandrou A. N., Duc E., and Entov V. Inertial, viscous and yield stress effects in Bingham fluid filling of a 2-D cavity. *Journal of Non-Newtonian Fluid Mechanics*, 96:383–403, 2001.

[30] Paradies C. J. and Rappaz M. Modeling the rheology of semisolid metal alloys during die casting. In *Modeling of Casting, Welding and Advanced Solidification Processes VIII. Proceedings of the 8th International Conference on Modeling of Casting and Welding Processes*, pages 933–940, San Diego, CA, June 7-12 1998. The Minerals, Metals and Materials Society, Edited by Thomas B. G. and Beckermann C.

[31] Koke J., Modigell M., Hufschmidt M., and Alexandrou A. A study on the die filling behavior with semisolid fluids. In *6th International Conference on Semisolid Processing of Alloys and Composites, Conference Proceedings*, pages 635–639, Turin, Italy, 27-29 September 2000.

[32] Georgiou G. C. *Singular finite elements for newtonian flow problems with stress singularities.* PhD thesis, The University of Michigan, Ann Arbor, MI, 1989.

[33] Housiadas K., Georgiou G. and Tsamopoulos J. The steady annular extrusion of a Newtonian liquid under gravity and surface tension. *International Journal for Numerical Methods in Fluids*, 33:1099–1119, 2000.

[34] Irons B. M. A frontal solution program for finite element analysis. *International Journal for Numerical Methods in Engineering*, 2:5, 1970.

[35] Walters R. A. The frontal method in hydrodynamics simulations. *Computers and Fluids*, 8:265, 1980.

[36] Boudouvis A. G. and Scriven L. E. Explicitly vectorized frontal routine for hydrodynamic stability and bifurcation analysis by Galerkin/finite element methods. In *Proc. Supercomp. Appl. Symp.*, Oct. 31-Nov. 1, 1984.

[37] Hood P. Frontal solution program for unsymmetric matrices. *International Journal for Numerical Methods in Engineering*, 10:379, 1976.

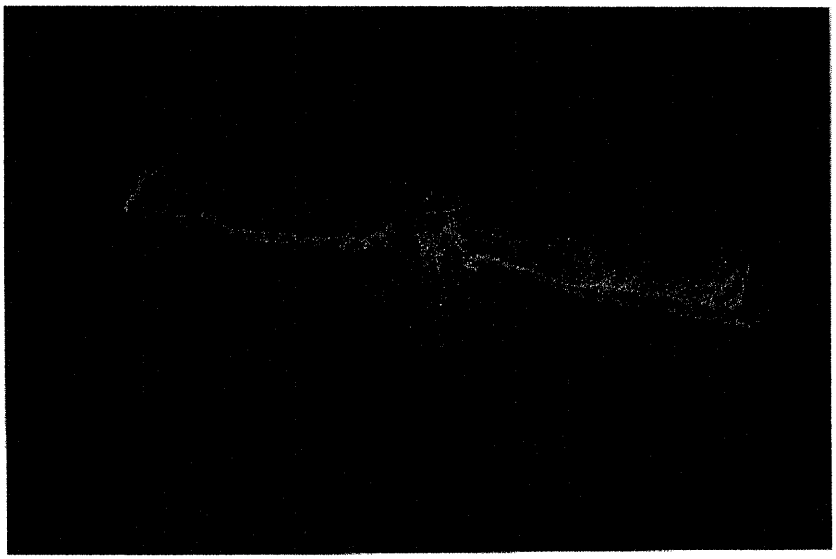

Figure 1: Flow instability in SSMP: toothpaste behavior (Courtesy of Aluminium Pechiney).

Figure 2: Flow instability in SSMP: toothpaste behavior (Courtesy of Aluminium Pechiney).

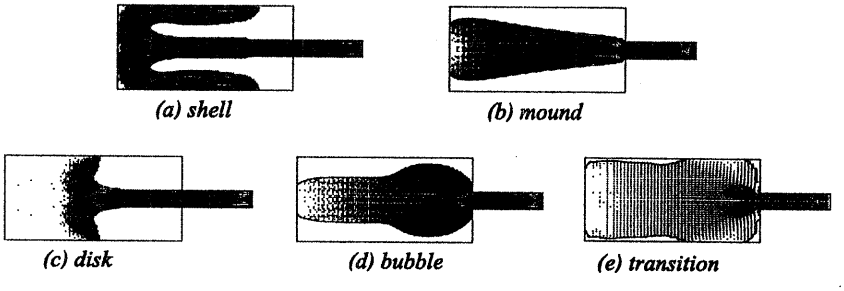

Figure 3: Summary of the flow patterns observed in 2-D die filling [29].

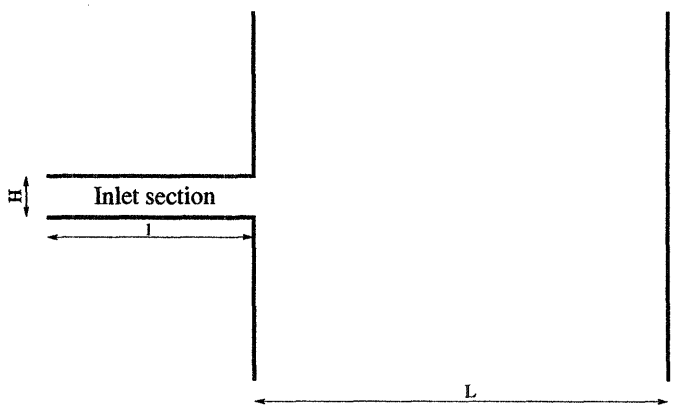

Figure 4: Geometry of the two-dimensional cavity (H, l, L).

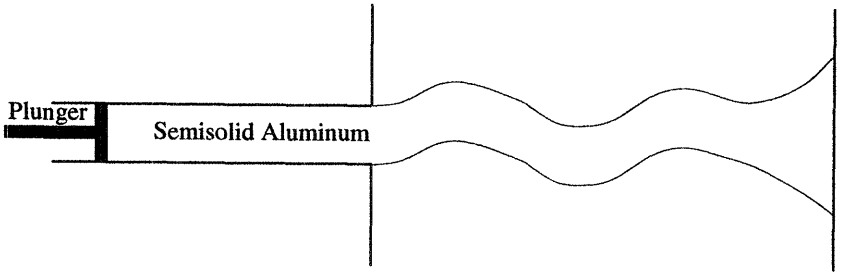

Figure 5: Schematic of the "toothpaste" behavior in a simple cavity.

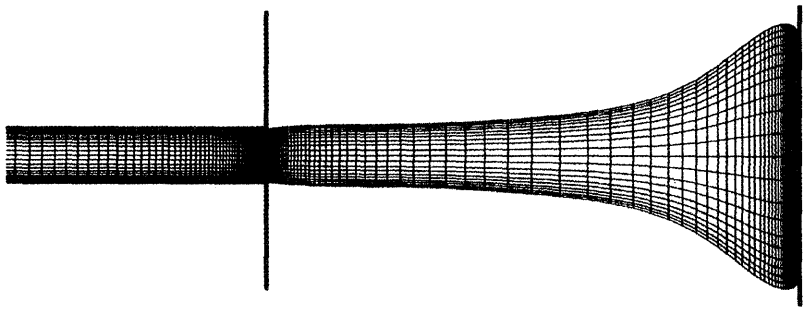

Figure 6: Geometry and finite element mesh.

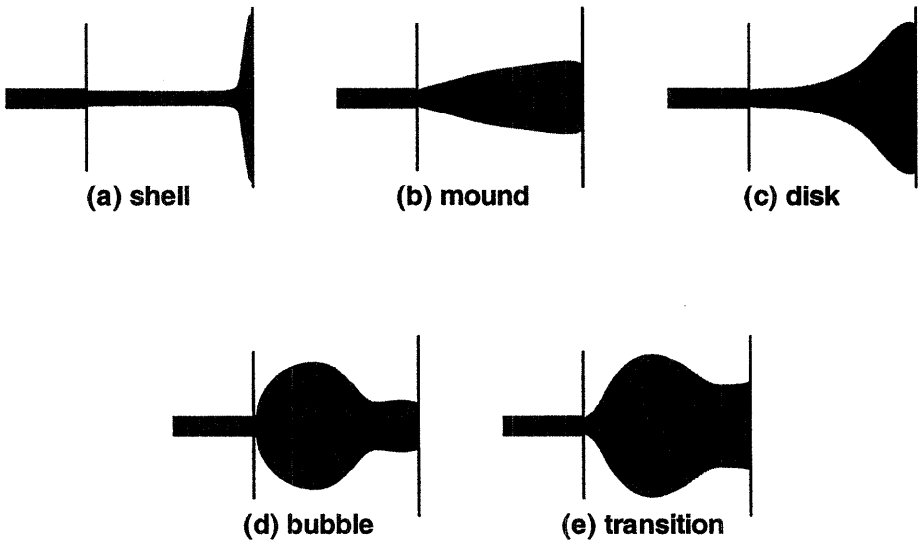

Figure 7: Summary of the flow patterns observed for the $L = 10$ geometry. Yielded and unyielded regions are highlighted.

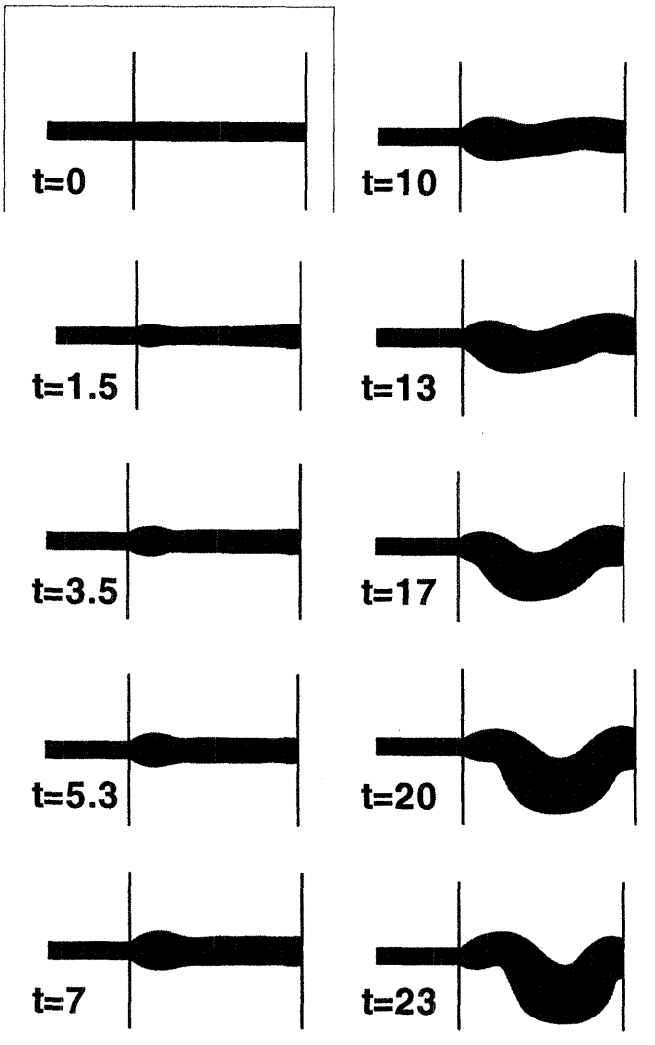

Figure 8: Toothpaste behavior, $Re = 1$, $Bi = 3$, $L = 10$. The disturbance is imposed from $t = 0$ until $t = 1.5$.

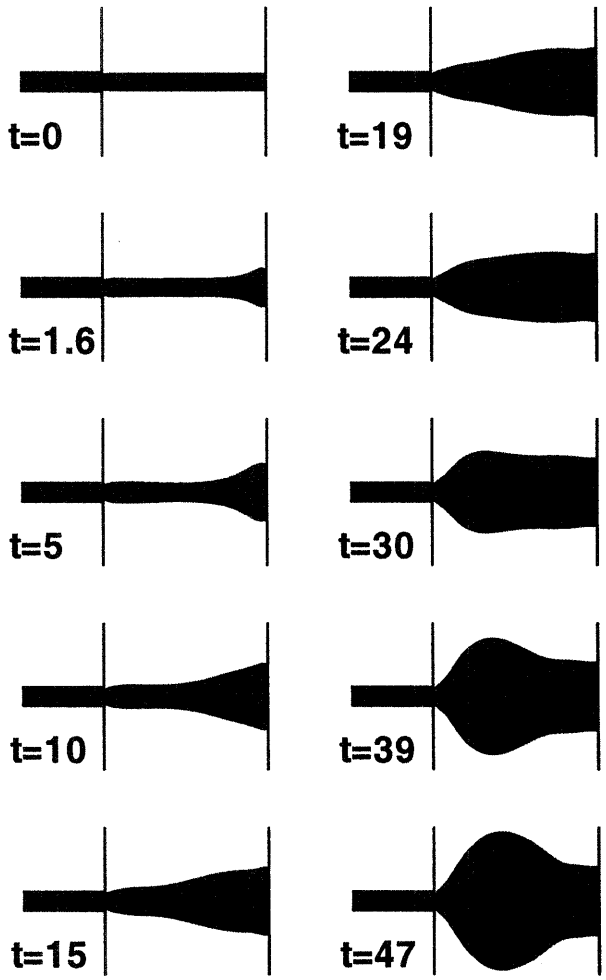

Figure 9: Stable jet behavior, $Re = 5$, $Bi = 1$, $L = 10$. The disturbance is imposed from $t = 0$ until $t = 1.5$.

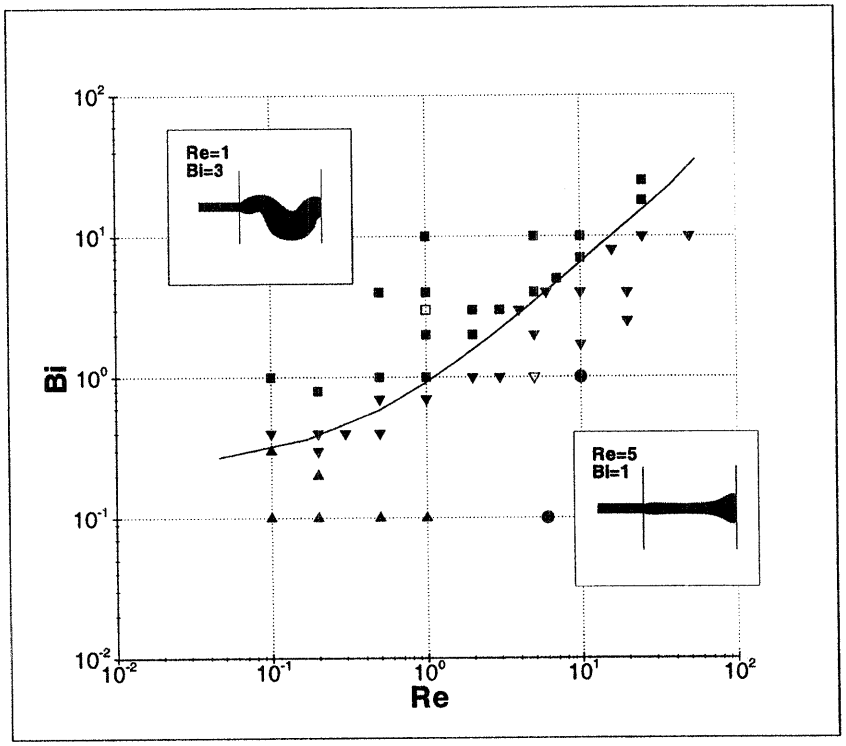

Figure 10: Stability of the jet when hitting a vertical suface ($L = 10$), the Reynolds and Bingham numbers being the control parameters. ▲-"mound" pattern; ●-"disk" pattern; ■-"bubble" pattern; ▼-"transition" pattern. The hollow symbols (□, and ▽) represent the cases discussed in detail and pictured on the map. The estimated boundary between the stable and unstable behaviors has been sketched in. Stable and unstable behaviors are respectively below and above this limiting line.

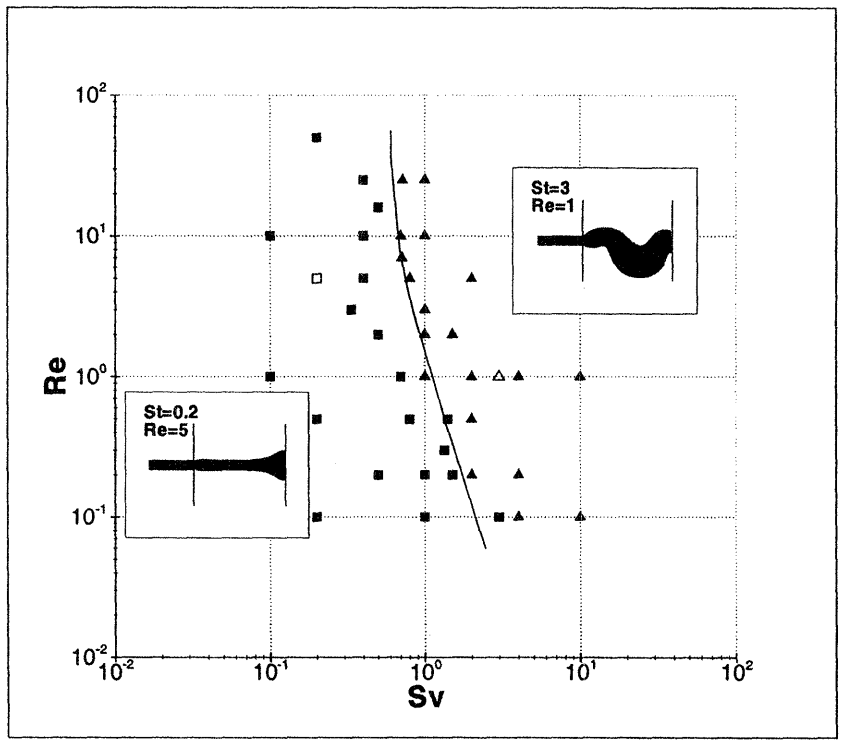

Figure 11: Stability of the jet when hitting a vertival surface ($L = 10$), the Saint-Venant and Reynolds numbers being the control parameters. ■-stable pattern; ▲-unstable pattern. The hollow symbols (□ and △) represent the cases pictured on the map. The estimated boundary between the two behaviors has been sketched in.

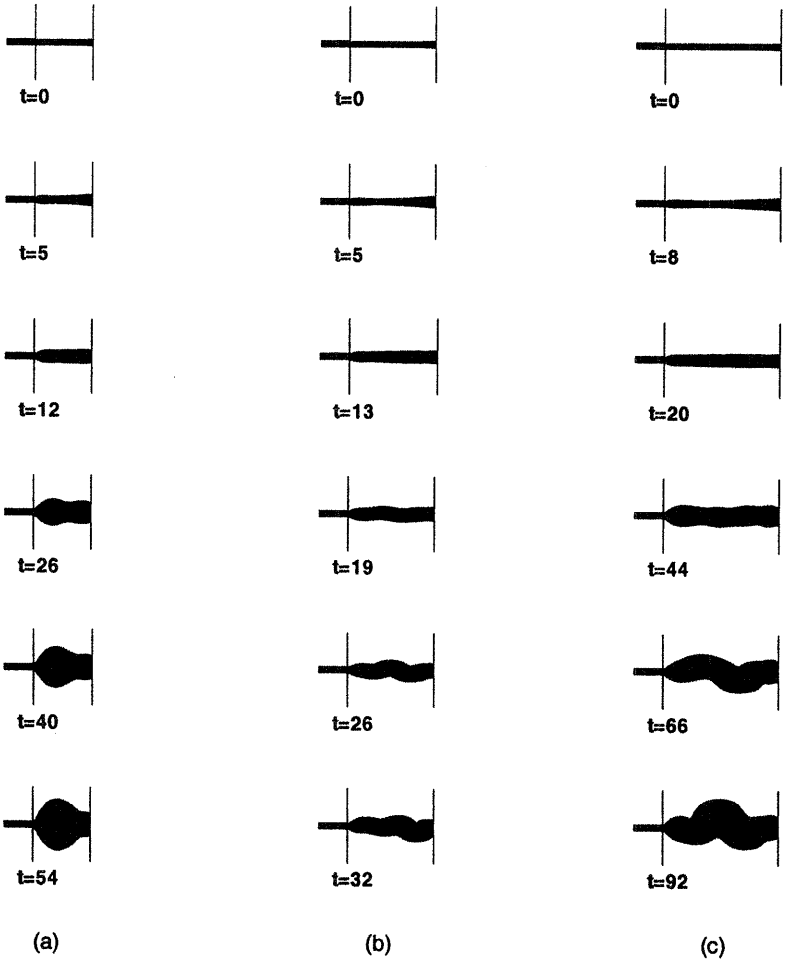

Figure 12: Stability of the flow ($Re = 1, Bi = 0.7$) for three different jet lengths. (a) $L = 10$, (b) $L = 15$, (c) $L = 20$.

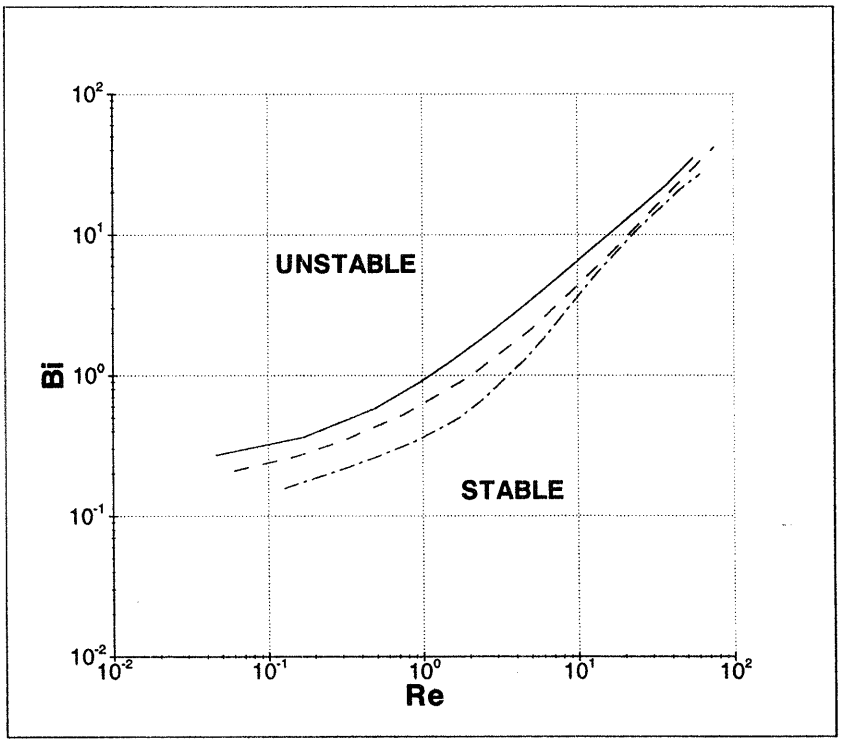

Figure 13: Estimated stability limits for different jet lengths. $L = 10$ (solid line), $L = 15$ (dashed line) and $L = 20$ (dashdotted line).

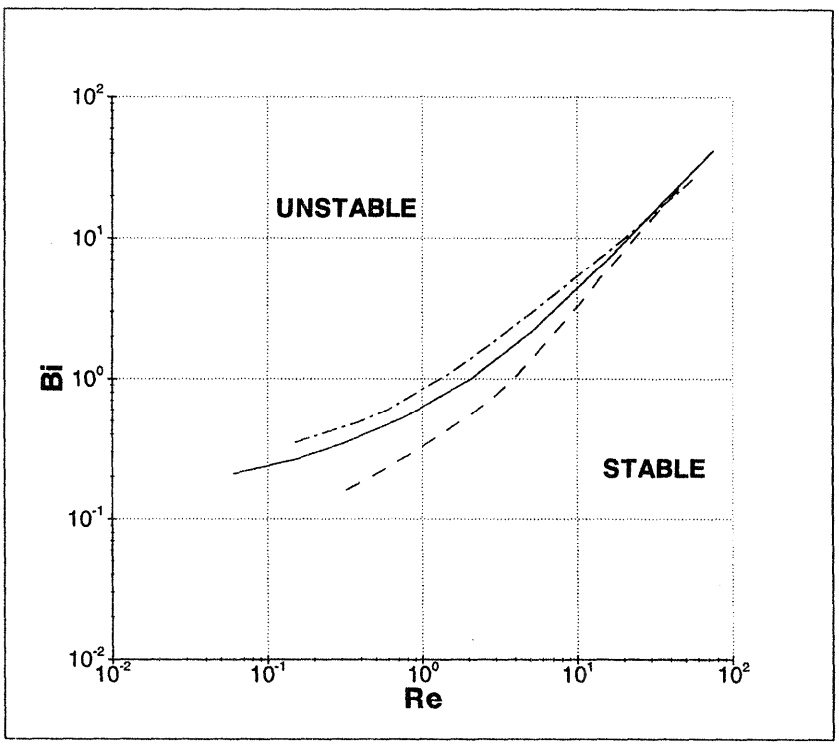

Figure 14: Estimated stability limits for different power-law coefficients. $n = 1$ (solid line), $n = 0.5$ (dashed line) and $n = 1.5$ (dashdotted line).

B. Quantitative Microstructure Characterization of Commercial Semi-Solid Aluminum Alloys

QUANTITATIVE MICROSTRUCTURE CHARACTERIZATION OF COMMERCIAL SEMI-SOLID ALUMINUM ALLOYS

Report PR-01-#2

Research Team:	Qingyue Pan	(508) 831 5790	qypan@wpi.edu
	Diran Apelian	(508) 831-5992	dapelian@wpi.edu
Focus Group:	Craig Bergsma		Northwest Aluminum
	Tom Caldwell		Madison-Kipp Corp.
	Ray Donahue		Mercury Marine
	Eric Erike		TRW
	John Jorstad		JLJ Technologies
	Steve Midson		Formcast
	Mike Thieman		THT Presses
	Per Arne Tondel		Elkem Aluminum
	Steve Udvardy		NADCA
	Jim Van Wert		Amcast
	Josef Woehrer		Salzburger Aluminum

PROJECT STATEMENT

Objectives

- Determine effect of processing temperature on microstructural evolution of semi-solid alloys during reheating.
- Determine effect of isothermal holding on microstructure evolution in the semi-solid state.
- Characterize differences in microstructure evolution of various semi-solid billets.
- Investigate formation mechanism of the entrapped liquid.
- Provide quantatitive data for optimization of industrial practice.

Strategy

- The rheological behavior and flow properties of semi-solid alloys depend on their microstructure developed during reheating. Thus an accurate

understanding of microstructure evolution during commercial processing conditions is critical for optimization and control of semi-solid processing.

- In this study, various semi-solid billets including MHD, GR (by addition of Ti-B or Si-B alloys), SIMA, new MIT and UBE processed materials were evaluated. Processing conditions investigated include different processing temperatures during continuous heating, as well as isothermal holding for different time at commercial forming temperatures.
- Image analysis was carried out to quantify the semi-solid microstructure. Three important characteristic parameters--shape factor, particle size of Alpha particles, as well as the amount of entrapped liquid within the Alpha phase were measured in this study.

ACHIEVEMENTS THIS QUARTER

During this quarter, extensive image analysis was carried out to quantify microstructure evolution of various semi-solid billets manufactured by MHD, GR (by addition of Ti-B or Si-B alloys), SIMA, new MIT and UBE processes, respectively. Detailed results are given as follows.

1. The chemically grain refined billets have relatively high entrapped liquid content. During commercial forming conditions, the entrapped liquid content usually accounts for 15-30% of the total liquid phase for grain refined billets, and 8-15% for SIMA and MHD billets.

2. The formation of the entrapped liquid can be attributed to the coalescence of the broken dendrite arms upon reheating. SEM analysis reveals that there are two types of entrapped liquid in nature. One is entrapped in isolation within the Alpha phase, and the other is entrapped in 2D but is connected to the intergranular eutectic in 3D. Specifically, we found that the isolated entrapped liquid consists of extremely fine eutectic grains (in order of several micrometers), and a lot of small oxide spheroids have been identified as the nuclei for the fine eutectic grains.

3. Higher processing temperature tends to decrease shape factor value and entrapped liquid content, however, it also increases the Alpha particle size and the runoff of liquid phase during semi-solid forming. A favorite temperature range for aluminum semi-solid billets is between 580-590°C. For grain refined billets, 585-590°C is recommended.

4. Isothermal holding leads to a speroidization and a coarsening process of Alpha particles. Analysis on quantitative data points out that an optimum

isothermal holding time is between 2-8 minutes. For grain refined billets, the upper limit is recommended.

5. Specifically, both processing temperature and isothermal holding have a significant influence on the entrapped liquid content of GR billets. Increasing processing temperature or isothermal holding time decreases entrapped liquid content of GR billets considerably. However, processing temperature and isothermal holding time show little effect on the entrapped liquid content of SIMA and MHD billets.

Appendix A is a detailed report on the quantitative microstructural characterization of various semi-solid billets.

CHANGES IN PROJECT STATEMENTS

None

WORK PLANNED FOR NEXT QUARTER

This project is completed.

Appendix A

QUANTITATIVE MICROSTRUCTURE CHARACTERIZATION OF COMMERCIAL SEMI-SOLID ALUMINUM ALLOYS

PR-01-#2

Qingyue Pan, and Diran Apelian,

Advanced Casting Research Center (ACRC)
Metal Processing Institute
WPI, Worcester, MA 01609

The rheological properties of semi-solid metal slurries are strongly dependent on their microstructure. Specifically, our previous studies identified that three characteristic microstructural parameters are critical in determining rheological behavior of aluminum semi-solid slurries. They are

1. Particle size of the Alpha phase,
2. Shape factor of the Alpha particles, and
3. Entrapped liquid content within the Alpha particles.

Using the MPI image analyzer, we quantified microstructual evolution of various semi-solid billets during commercial forming conditions. In report PR-01-#1, we presented our results on A356 billets manufactured by both MHD and GR processes. This report presents our recent results on new MIT, SIMA (strain-induced melt activation), SiBloy (grain refined by addition of Si-B alloys) and UBE materials. Specifically, we compared the quantitative data of all these materials during commercial processing conditions, including continuous heating and isothermal holding at a commercial forming temperature. Therefore, this report provides a comprehensive knowledge base in understanding the effect of processing conditions and material genealogy on the microstructure evolution and rheological properties of various semi-solid metal slurries.

1. EXPERIMENTAL

1.1 Materials

The semi-solid billets evaluated include MHD, GR (by addition of Ti-B or Si-B alloys), SIMA, new MIT, as well as UBE processed materials. Table 1 lists alloy designations and composition. Sliced samples with approximately 0.25-inch

thickness each were cut directly from the billets. Figure 1 illustrates the experimental procedures.

Table I: Chemical composition of the alloys investigated

Alloy	Composition, %				
	Si	Mg	Cu	Mn	Fe
A356 (MHD)	6.92	0.18	0.09	0.05	0.1
A356 (GR)	6.85	0.33	0.11	0.05	0.1
SiBloy (GR)	6.84	0.29	0.0005	0.003	0.07
A357 (SIMA)	6.61	0.53	--	0.01	0.1
A356 (MIT)	7.27	0.38	0.01	---	0.1
Al-Si-Cu (UBE)	---	---	---	---	---

1.2 Processing Conditions

Processing conditions investigated in this study include continuous heating and quenching samples at different temperatures in the two-phase region, as well as isothermal holding at 582°C and quenching samples at different holding time, as shown in Figure 2.

The ***first series*** of experiments dealt with the effect of processing temperature on semi-solid microstructure during continuous heating in the semi-solid state. The average heating rate was about 49^0C/min.

The ***second series*** of experiments were designed to investigate the effect of isothermal hold on microstructural evolution at a temperature commonly used in commercial forming operations (582°C). Holding time varied from 1 to 64 minutes.

1.3 Microstructure Characterization

Metallographic observations were made on the water-quenched samples. The specimens were etched with Keller's reagent after mounting, grinding, and polishing.

Microstructure characterization was performed using optical microscopy and image analyzer (microGOP2000/S). Three specific microstructural parameters

were measured to quantitatively characterize the semisolid microstructures. They are

1. particle size of the Alpha phase, *D*
2. shape factor of the Alpha particles, *SF*
3. entrapped liquid content within the Alpha particles, V_f

The particle size (*D*) is determined by

$$D = 2 \times \sqrt{\frac{A}{\pi}} \tag{1}$$

Where *A* is the area of the particle. The average particle size is the mean value of the total numbers of particles measured.

The shape factor (*SF*) is defined as

$$SF = \frac{P^2}{4\pi A} \tag{2}$$

Where *P* is the perimeter of the particle. For a perfectly globular shape, *SF* is equal to 1. The more irregular the particles, the higher the shape factor value. The shape factor values reported here are the mean values of the total numbers of particles measured.

Specifically, we found that there are two types of entrapped liquid in nature. One is entrapped within Alpha particles in isolation, and the other is entrapped within the Alpha particles in 2D, but is connected to the intergranular eutectic in 3D. The entrapped liquid content (V_f) here is defined as

$$V_f = \frac{A_{EL}}{A_{Liquid}} \times 100\% \tag{3}$$

Where A_{EL} is the area of the entrapped liquid in isolation, A_{Liquid} is the area of the entire liquid phase including the intergranular eutectic phase, the entrapped liquid in isolation, as well as the entrapped liquid in connection to the intergranular eutectic. Since most entrapped liquid has a spherical shape, here the mean entrapped liquid content in 2D can be considered as an approximate volume fraction value in 3D.

In order to obtain results of statistical significance, more than twelve images were measured for each sample. In addition, since there is significant difference in

microstructural scale throughout MHD A356, GR A356 and SiBloy as-cast billets, we analyzed semi-solid microstructures at twelve different locations on the cross section, which cover the whole region within a radius.

2. RESULTS & ANALYSIS

Microstructural evolution of various semi-solid billets as a function of material genealogy and processing temperature is presented below in section 2.1. Microstructure evolution as a function of material genealogy and isothermal holding time at 582°C is presented in section 2.2. This is followed by analysis on formation mechanism of the entrapped liquid within the Alpha phase.

2.1 Microstructural Evolution During Continuous Reheating

From a rheological standpoint, an "ideal" semi-solid microstructure is composed of small, round Alpha particles containing no entrapped liquid and homogeneously distributed in a eutectic phase, as illustrated in Figure 3. The small size of the Alpha particles is beneficial for the casting of thin-walled parts, while a more spherical shape, and the absence of entrapped liquid are critical for the improvement of the slurry flow properties during die filling.

Figure 4 compares typical as-cast microstructures of various semi-solid billets. It can be seen that their as-cast microstructures are quite different. The as-cast microstructure of GR billets (by addition of Ti-B or Si-B alloys) is a dendritic structure with a very fine scale, while the microstructure of MHD billets is a mixture of dendritic and rosette-like structures. SIMA billets show typical deformed microstructure with a lot fine Mg_2Si particles. The new MIT processed billets, however, have a globular Alpha structure, which is formed due to a rapid mechanical stirring and a strict cooling rate control during billet casting.

Upon reheating, the above billets show quite different microstructural evolution. Figures 5 and 6 give the typical semi-solid microstructures of all these billets at 580°C and 585°C, respectively. Visually, there are significant differences among them in terms of the shape and size of the Alpha particles, as well as the entrapped liquid content within the Alpha phase. Detailed image analysis results are given below.

2.1.1 Entrapped Liquid Content

The entrapped liquid within the Alpha phase has a significant influence on the rheological behavior of semi-solid slurry. As the entrapped liquid does not participate in the deformation during die filling, it has the effect of decreasing "effective" liquid fraction, and thus flow properties.

Figure 7 details the evolution of entrapped liquid as a function of processing temperature and material genealogy. It can be seen that

- GR billets (by addition of Ti-B or Si-B alloys) have much higher entrapped liquid content than MHD billets. The entrapped liquid content in Ti-B refined billets can account for as high as 36% of the liquid phase at 578°C. During commercial forming temperature range between 580-590°C, the entrapped liquid content in GR billets varies between 15-30%, which is 2-3 times higher than in MHD billets

- Processing temperature has a significant influence on the entrapped liquid content of GR billets. With increasing temperature, the entrapped liquid content decreases dramatically, however, processing temperature shows little effect on the entrapped liquid content of MHD and SIMA billets.

- No entrapped liquid was found in MIT and UBE processed billets.

2.1.2 Particle Size

Figure 8 details the evolution of particle size as a function of processing temperature and material genealogy. The quantitative data shows that

- Higher processing temperature tends to increase particle size, but the effect is not significant in commercial forming temperature range (580-590°C).

- The Alpha particle size in grain refined billets (by addition of Ti-B or Si-B alloys) is much larger than in MHD, SIMA and MIT processed billets. Among them, the SIMA billets have the smallest Alpha particle size, and very uniform size distribution, falling in the range between 50-80 μm in the temperature range investigated.

- Interestingly, processing temperature has no influence on Alpha particle size of Si-B grain refined billets (SiBloy). In addition, compared to Ti-B grain refined billets (GR A356), the particle size distribution in Si-B refined billets is more uniform.

2.1.2 Shape Factor

Figure 9 details the evolution of shape factor as a function of processing temperature and material genealogy. It can be seen that

- During commercial forming temperature range (580-590°C), shape factor values of all the semi-solid billets decrease with increasing temperature, indicating that higher forming temperature leads to a better spheriodization of Alpha particles.

- As shown in Figure 9, SIMA billets have the smallest shape factor value, corresponding to the best spheroidized Alpha particles. Whereas, Si-B refined billets have the highest shape factor value, thus corresponding to the most irregular shape of Alpha particles. This is consistent with microstructure observations.

2.2 Microstructural Evolution During Isothermal Holding at 582°C

Figures 10 and 11 give the semi-solid microstructures of various billets isothermal holding for 2 minute, and 32 minute, respectively. A rapid evolution of Alpha particles towards a globular structure was seen in MHD, SIMA and MIT billets, whereas relatively slow spheroidization was observed in GR billets. This can be clearly seen from the image analysis results given below.

2.2.1 Entrapped Liquid Content

Figure 12 gives the evolution of entrapped liquid content as a function of isothermal holding time and material genealogy. The results show that

- Isothermal holding has a significant effect on the entrapped liquid content of GR billets (by addition of Ti-B or Si-B alloys). With increasing isothermal holding time, the entrapped liquid content decreases considerably.

- Isothermal holding, however, shows little influence on the entrapped liquid content of MHD and SIMA processed billets. Again, no entrapped liquid was found in MIT processed billets under isothermal holding conditions.

2.2.2 Particle Size

Figure 13 gives the evolution of particle size as a function of isothermal holding time and material genealogy.

- As expected, isothermal holding leads to coarsening of Alpha particles. Specifically, a good linear dependence between particle size and isothermal holding time was found in GR (by addition of Ti-B alloys), MHD, MIT and SIMA processed billets.

- Interestingly, isothermal holding does not show any influence on the particle size of Si-B refined billets. With increasing isothermal holding time, the particle size of Si-B refined billets tends to a constant value (around 160 μm), even isothermal holding for 64 minutes.

- The insensitivity of particle size in Si-B grain refined billets to both processing temperature and isothermal holding time is most likely related to the long-term grain refinement effect of Si-B alloys found by ACRC researchers.

2.2.3 Shape Factor

Figure 14 gives the evolution of shape factor as a function of isothermal holding time and material genealogy. It can be seen that

- A rapid spheroidization process usually occurs in the first 1-2 minute isothermal holding, and thereafter, the process proceeds very slowly.

- Si-B and Ti-B grain refined billets have higher shape factor values than the other billets, corresponding to a more irregular shape of Alpha particles. Moreover, isothermal holding shows little effect on the spheroidization of Alpha particles in GR billets, particularly for Si-B grain refined billets.

- Specifically, a significant difference in shape factor values has been observed throughout the grain refined billets. Usually, the microstructures at billet center have higher shape factor values than those at billet edge, indicating that the speroidization process at billet center is relatively slow.

2.3 Entrapped Liquid Analysis

As stated before, the entrapped liquid within the Alpha particles does not participate in the deformation during die filling, thus it greatly decreases the flow properties of the semi-solid slurry. Moreover, since no feeding is available during the subsequent solidification process, the entrapped liquid may cause casting defects such as microporosity, shrinkage etc. Therefore, an understanding of origin and nature of the entrapped liquid is critical.

Figures 15 through 16 show typical morphologies of the entrapped liquid within the Alpha phase under both microscope and SEM. It is clear that

- The entrapped liquid has different morphologies (see Figure 15). One typical morphology is circular. Others include irregular shapes such as triangle, rectangular or ellipse, etc.

- The morphology and amount of the entrapped liquid is strongly dependent on the as-cast microstructure of the billet. A fine dendritic as-cast structure tends to form high volume of entrapped liquid with both circular and irregular shapes, while a rosette-like as-cast structure gives rise to intermediate volume of globular entrapped liquid. If the as-cast billet has a spherical Alpha phase (for example, the MIT billet), one can obtain semi-solid microstructure completely free of the entrapped liquid upon reheating (compare Figure 4d with Figures 5d and 6d).

- Specifically, SEM observations clearly show that there are two types of entrapped liquid in nature. As shown in Figure 16(a), one is entrapped in isolation within the Alpha particles, and the other is entrapped in 2D but is connected to the intergranular eutectic in 3D. This can be easily identified by a comparison between the entrapped liquid and the intergranular eutectic. In fact, the entrapped liquid, which is connected to the intergranular eutectic in 3D, has exactly the same morphology as the intergranular eutectic phase.

- More importantly, an enlarged view of the entrapped liquid in isolation reveals that the entrapped liquid indeed consists of many extremely fine eutectic grains, as shown in Figure 16(b). The grain size is in order of several micrometers.

- Further SEM and EDAX analysis points out that there are many small oxide spheroids inside each eutectic grain, as shown in Figure 16(c). The small spheroids serve as nuclei for eutectic grains, thus leading to the formation of the extremely fine eutectic grains.

Based on the above observations, it is logical to assume that the origin of the entrapped liquid is due to the coalescence of the broken dendritic arms formed either by MHD or grain refinement treatment. Compared to rosette-like structure, the fine dentritic structure tends to entrap more liquid and form more irregular shapes during the coalescence upon reheating, and that's why the GR billets have much more entrapped liquid, and the entrapped liquid has more irregular shapes than MHD billets.

Obviously, our findings clarify some conflicting claims as to whether the entrapped liquid is connected to the rest of the eutectic or it is entrapped in isolation. Still, there are some issues remaining open.

- Where do the oxide spheroids come from? They come from the broken oxide film during billet casting? or from the oxidization due to the addition of Sr?

- Specifically, we observed that most modified eutectic silicon grows from the oxide films. Is this a new mechanism for modification of the eutectic silicon?

Further experiments are being carried out to try to answer these questions.

3. CONCLUSIONS

Based on our extensive microstructural observations and quantitative data, the following conclusions were drawn:

1. The chemically grain refined billets have relatively high entrapped liquid content. During commercial forming conditions, the entrapped liquid content usually accounts for 15-30% of the total liquid phase for grain refined billets, and 8-15% for SIMA and MHD billets.

2. The formation of the entrapped liquid can be attributed to the coalescence of the broken dendrite arms upon reheating. SEM analysis reveals that there are two types of entrapped liquid in nature. One is entrapped in isolation within the Alpha phase, and the other is entrapped in 2D but is connected to the intergranular eutectic in 3D. Specifically, we found that the isolated entrapped liquid consists of extremely fine eutectic grains (in order of several micrometers), and a lot of small oxide spheroids have been identified as the nuclei for the fine eutectic grains.

3. Higher processing temperature tends to decrease shape factor value and entrapped liquid content, however, it also increases the Alpha particle size and the runoff of liquid phase during semi-solid forming. A favorite temperature range for aluminum semi-solid billets is between 580-590°C. For grain refined billets, 585-590°C is recommended.

4. Isothermal holding leads to a speroidization and a coarsening process of Alpha particles. Analysis on quantitative data points out that an optimum isothermal holding time is between 2-8 minutes. For grain refined billets, the upper limit is recommended.

5. Specifically, both processing temperature and isothermal holding have a significant influence on the entrapped liquid content of GR billets. Increasing processing temperature or isothermal holding time decreases entrapped liquid content of GR billets considerably. However, processing temperature and isothermal holding time show little effect on the entrapped liquid content of SIMA and MHD billets.

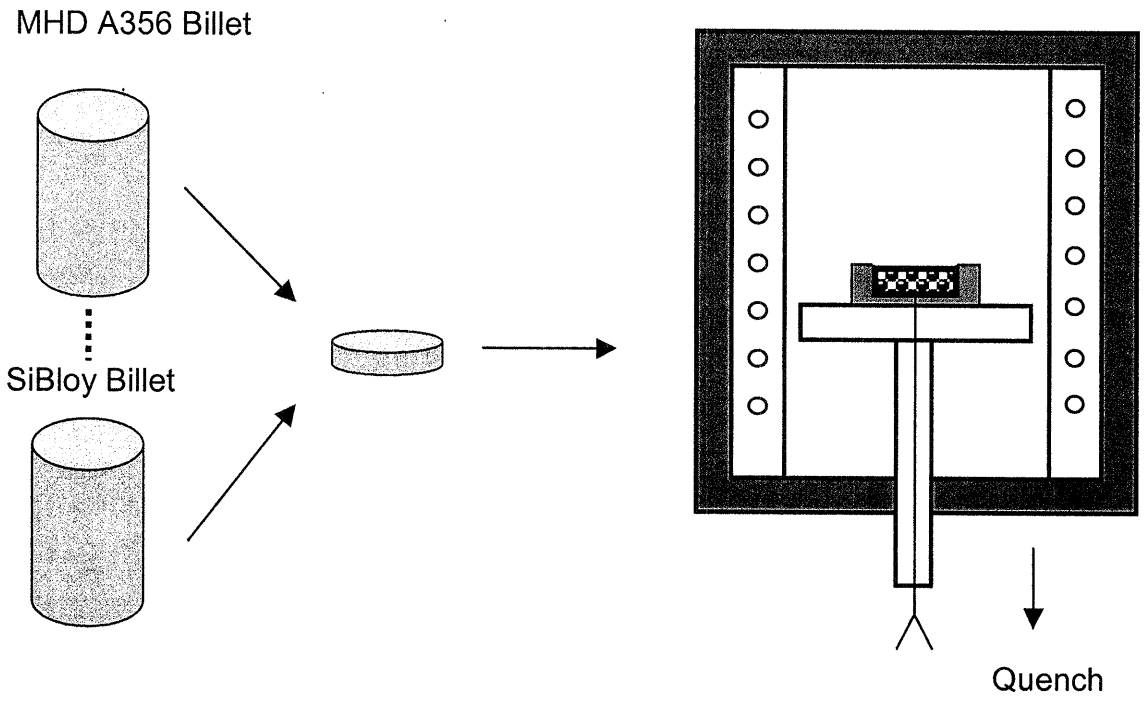

Figure 1: Schematic diagram of experimental procedures.

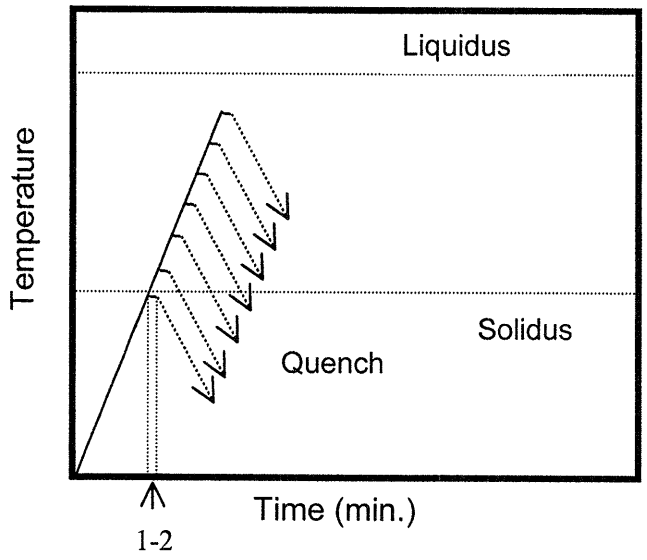

Figure 2 (a)

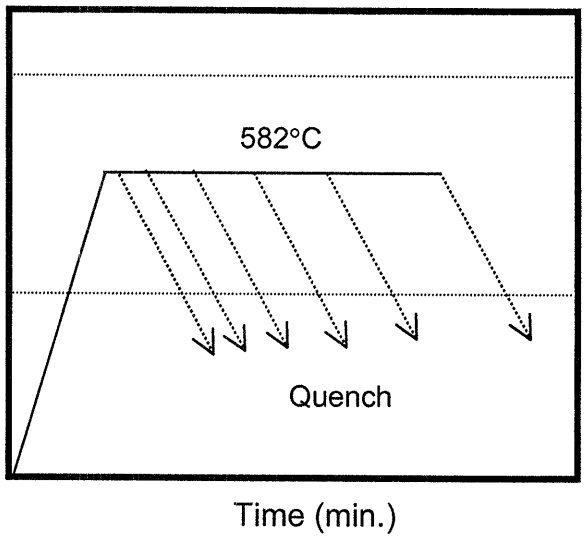

Figure 2 (b)

Figure 2: Schematic diagram of thermal treatments applied, (a) continuous reheating, and (b) isothermal holding.

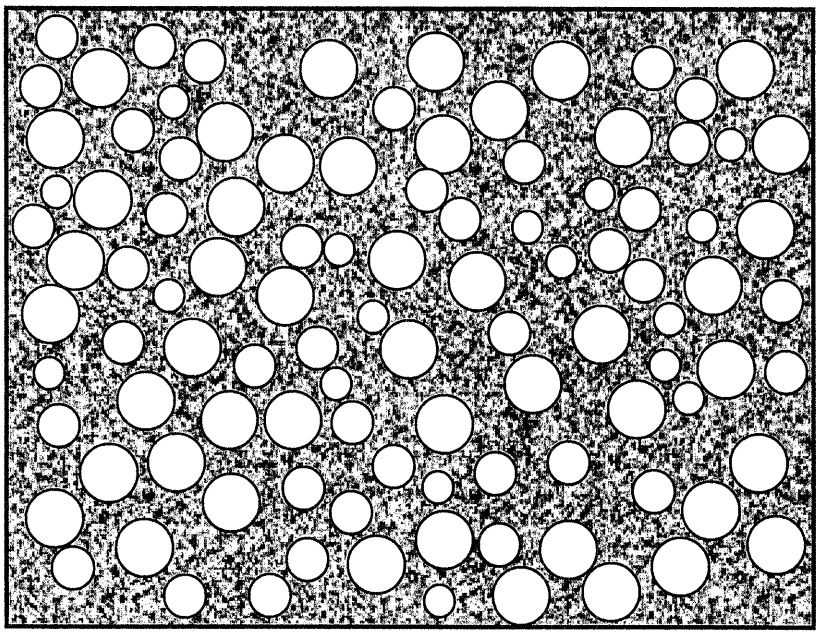

Figure 3: Schematic diagram of an “ideal” semi-solid structure.

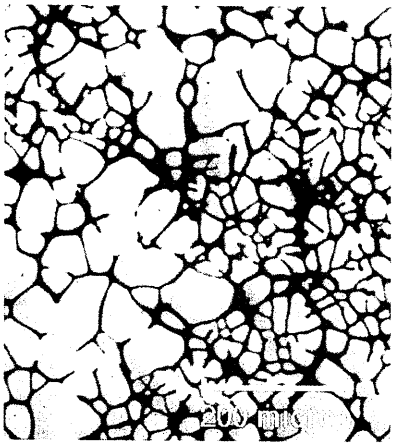

(a) MHD A356

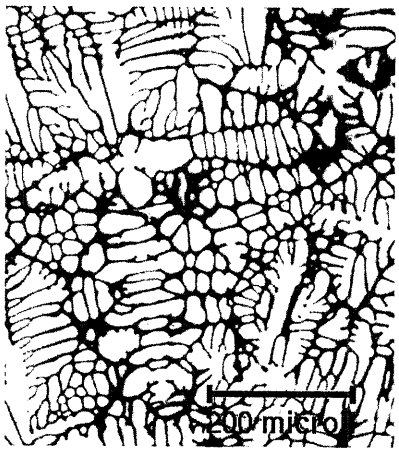

(b) GR A356

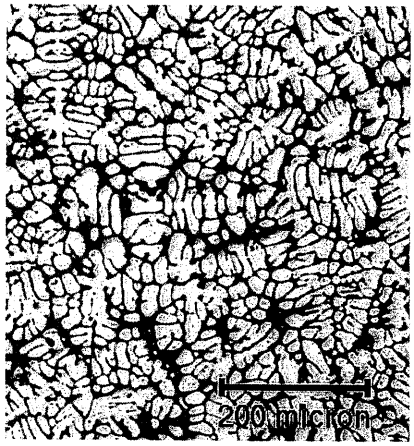

(c) SiBloy

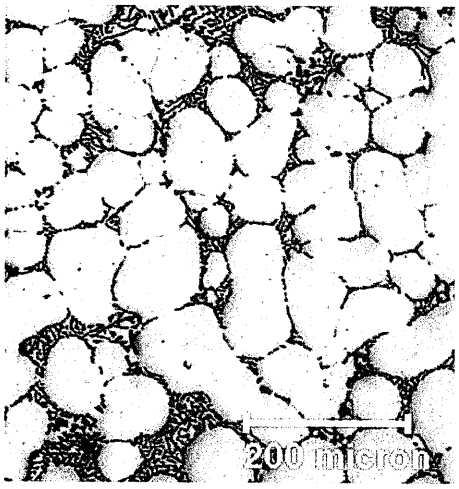

(d) MIT A356

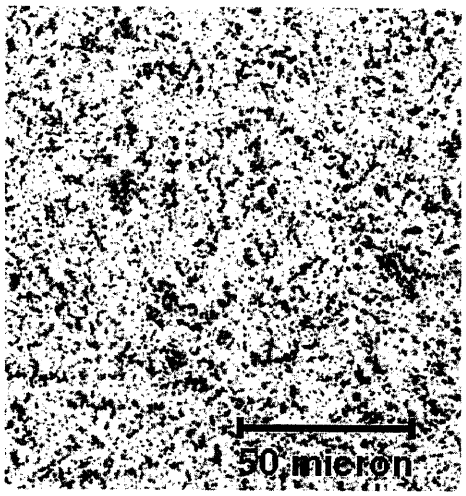

(e) SIMA 357

Figure 4: As-cast microstructure of various semi-solid billets.

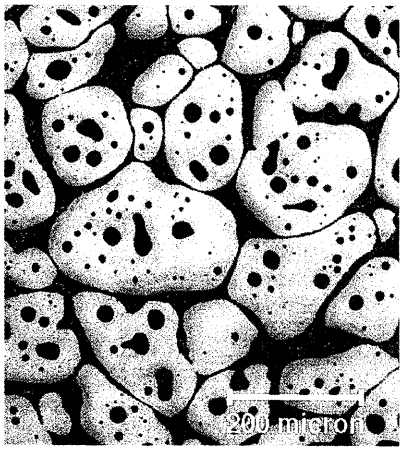

(a) MHD A356

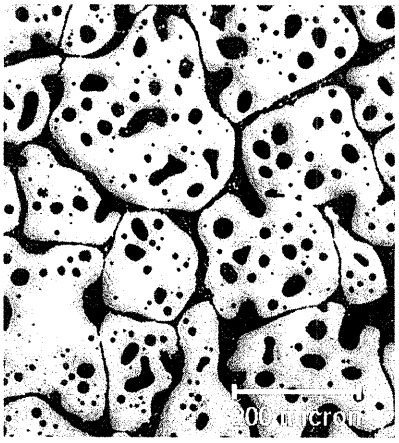

(b) GR A356

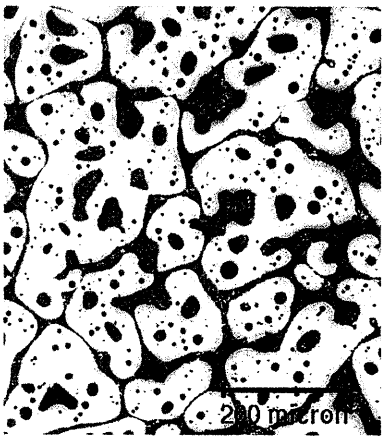

(c) SiBloy

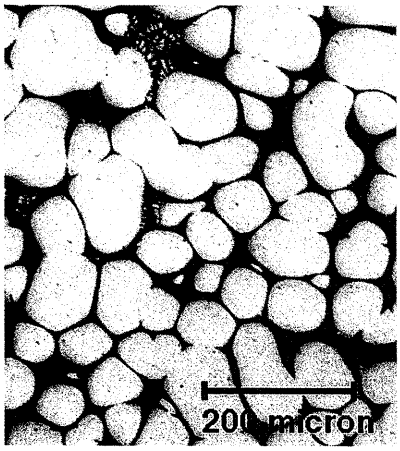

(d) MIT A356

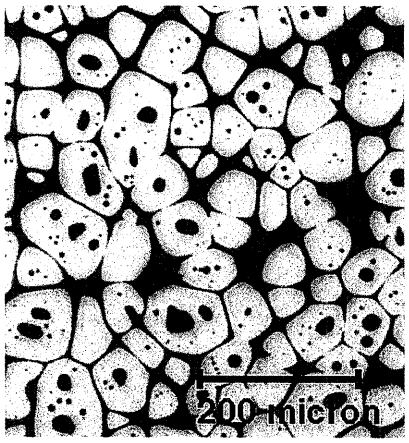

(e) SIMA A357

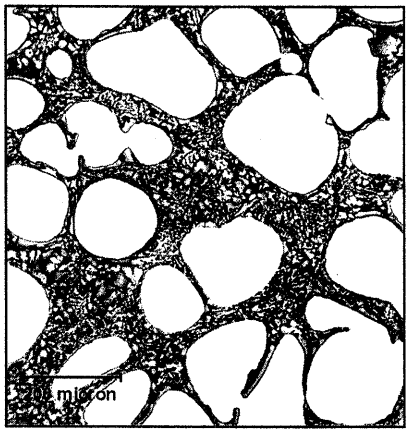

(f) UBE (Al-Si-Cu)

Figure 5: Semi-solid microstructure of various billets at 580°C.

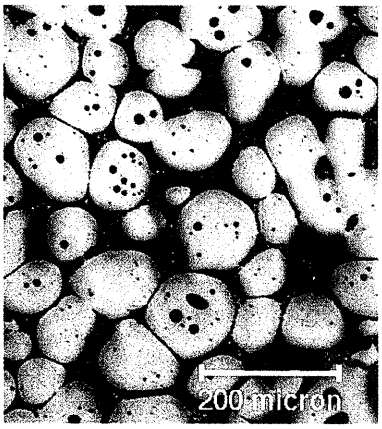

(a) MHD A356

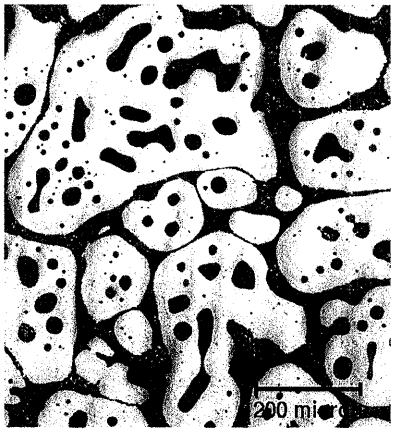

(b) GR A356

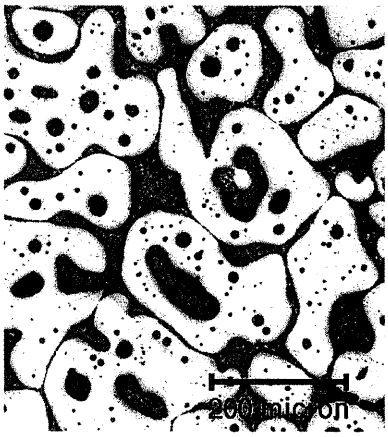

(c) SiBloy

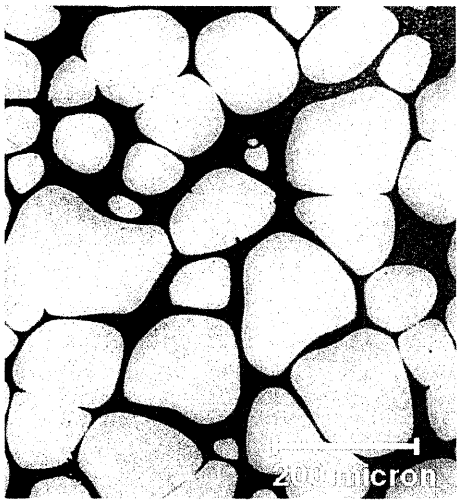

(d) MIT A356

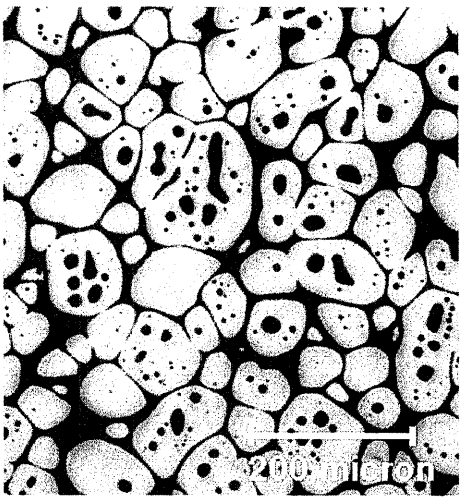

(e) SIMA 357

Figure 6: Semi-solid microstructure of various billets at 585°C.

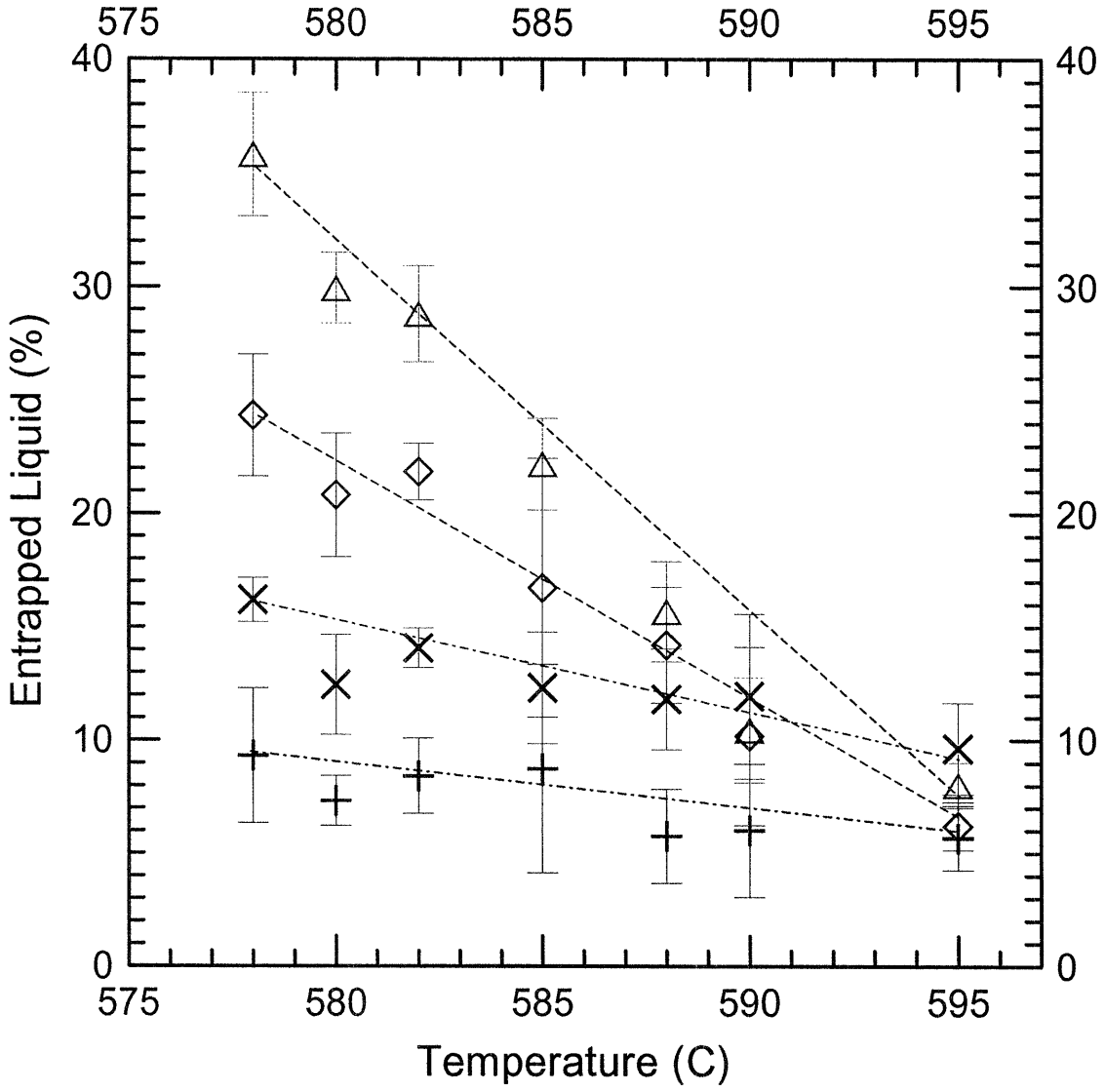

Figure 7: Evolution of entrapped liquid content as a function of processing temperature and material genealogy.

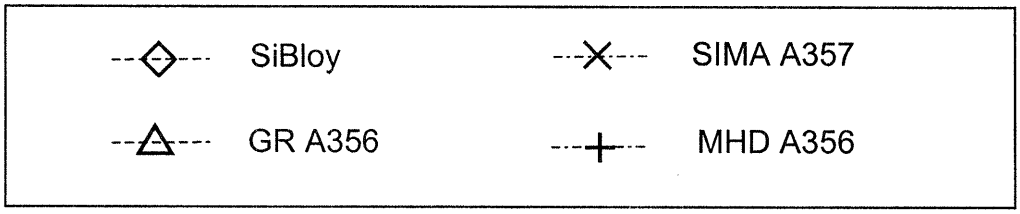

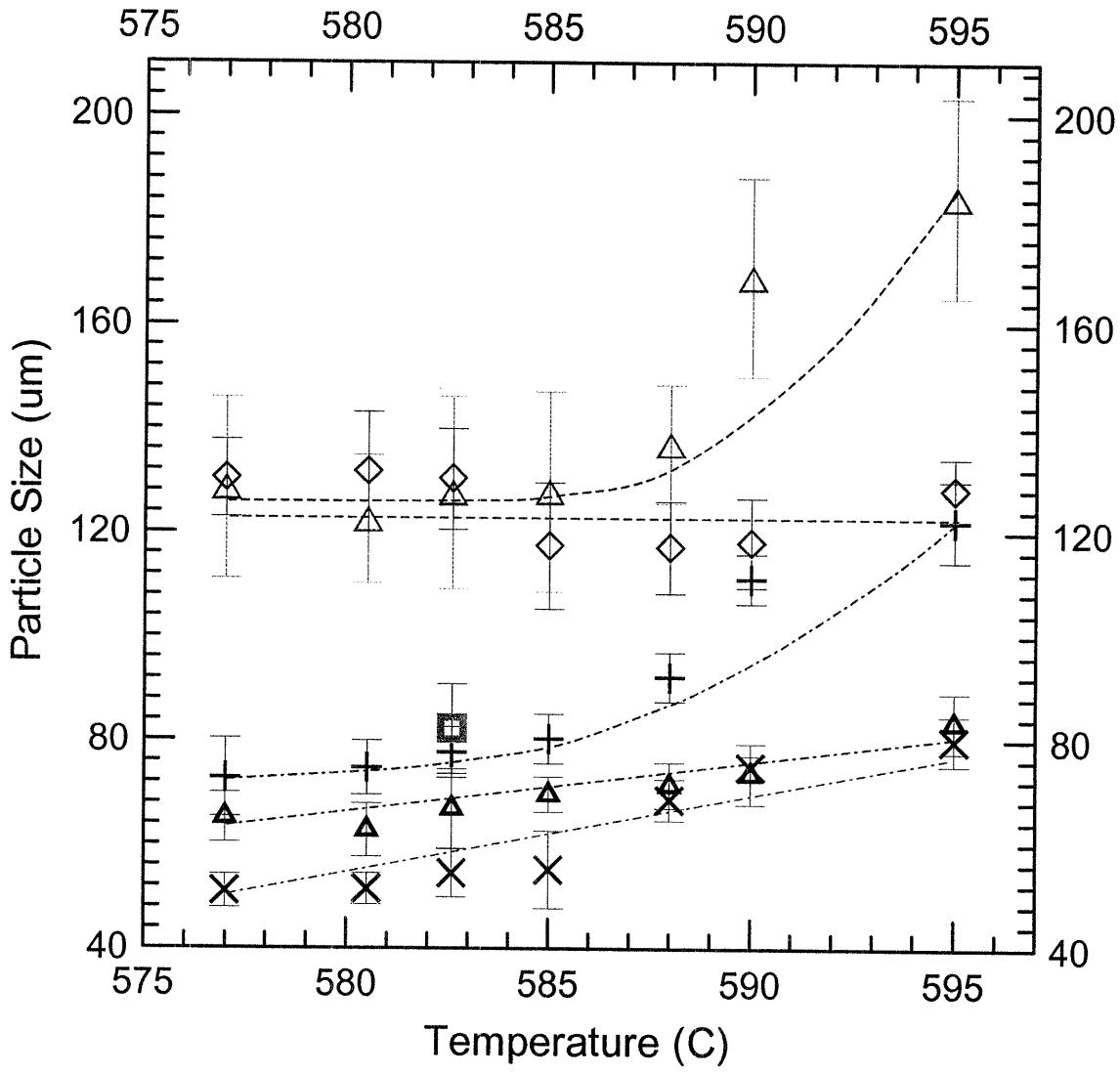

Figure 8: Evolution of particle size as a function of processing temperature and material genealogy.

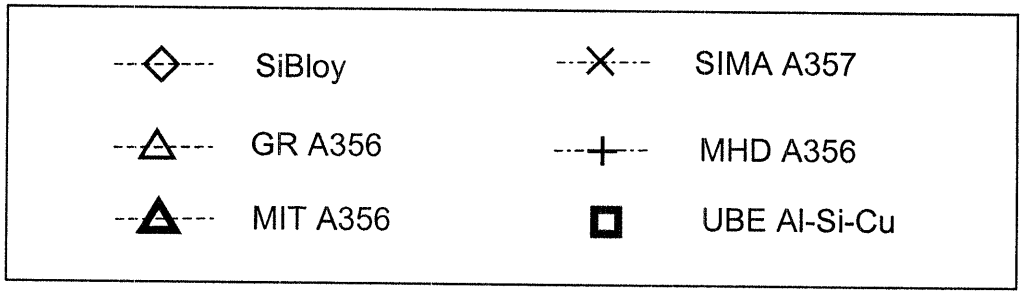

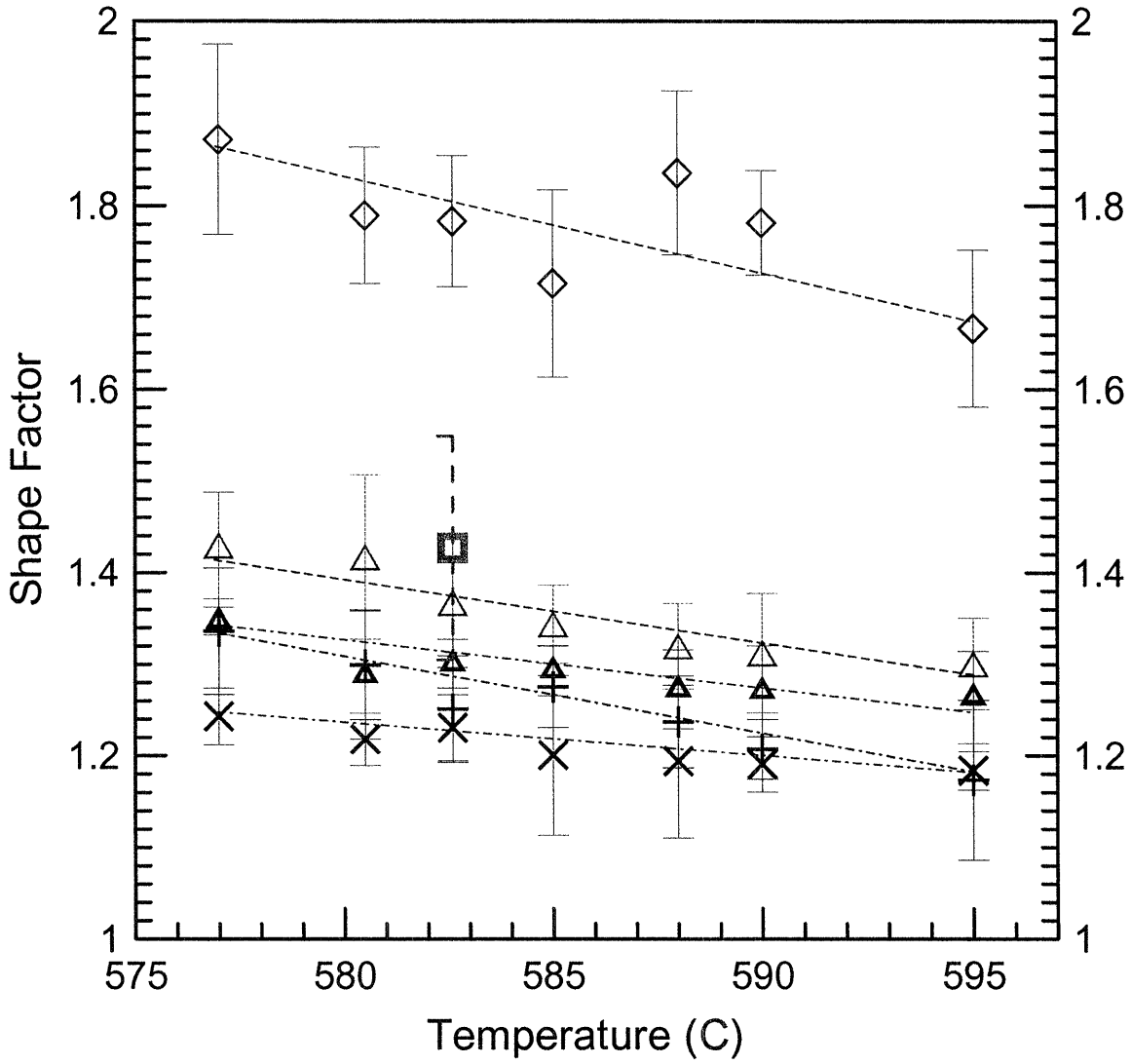

Figure 9: Evolution of shape fator as a function of processing temperature and material genealogy.

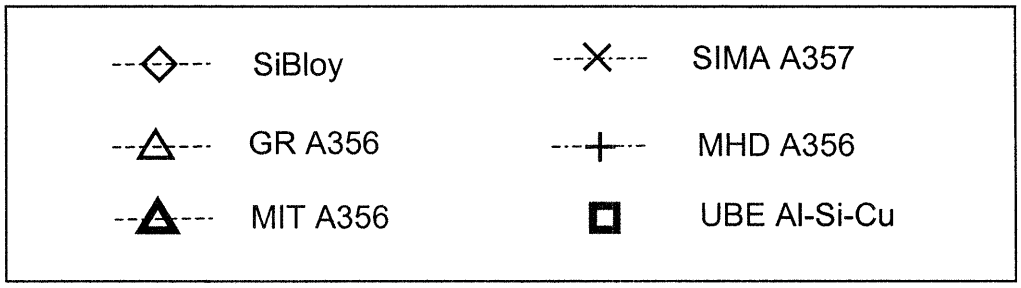

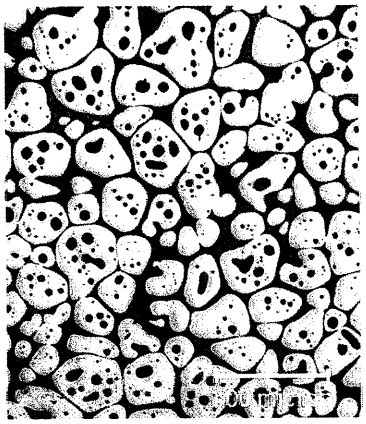

(a) MHD A356

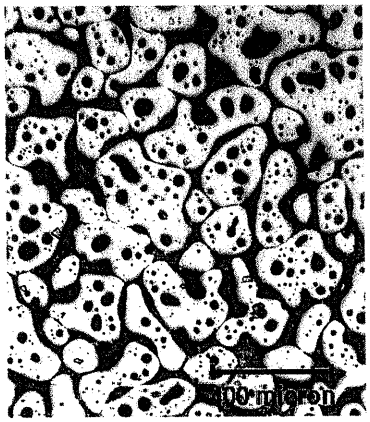

(b) GR A356

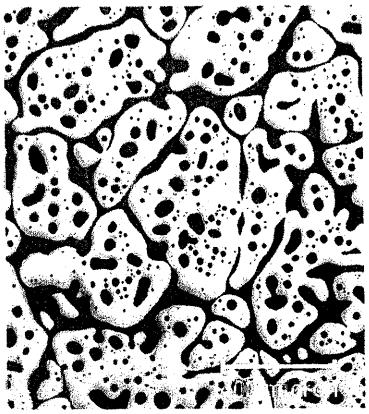

(c) SiBloy

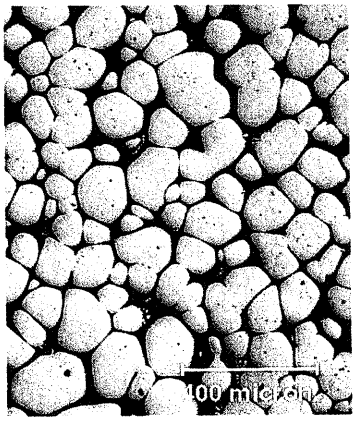

(d) MIT A356

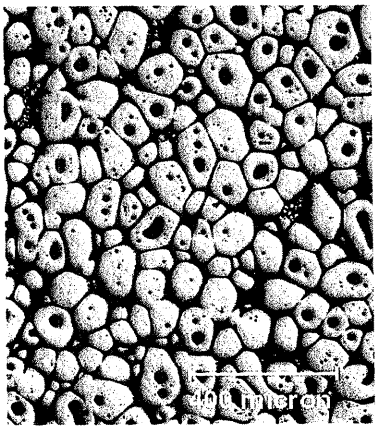

(e) SIMA 357

Figure 10: Semi-solid microstructure of various billets at isothermal holding for 2 minutes at 582°C .

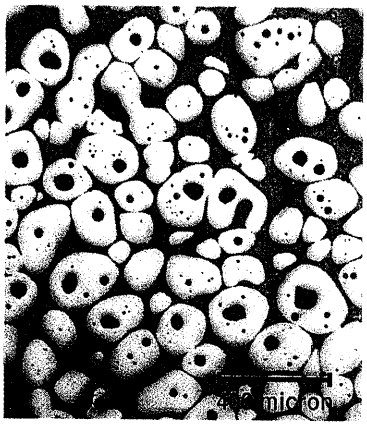

(a) MHD A356

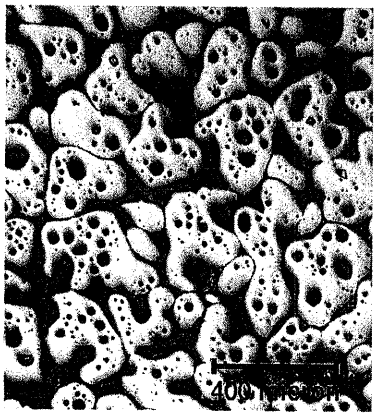

(b) GR A356

(c) SiBloy

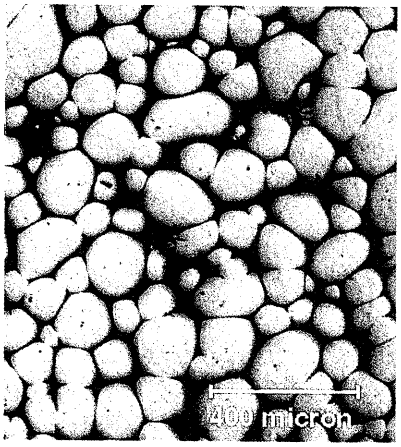

(d) MIT A356

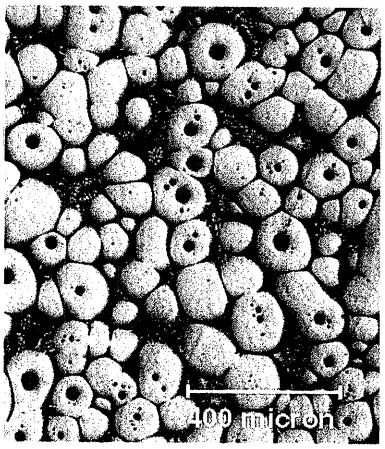

(e) SIMA 357

Figure 11: Semi-solid microstructure of various billets at isothermal holding for 32 minutes at 582°C .

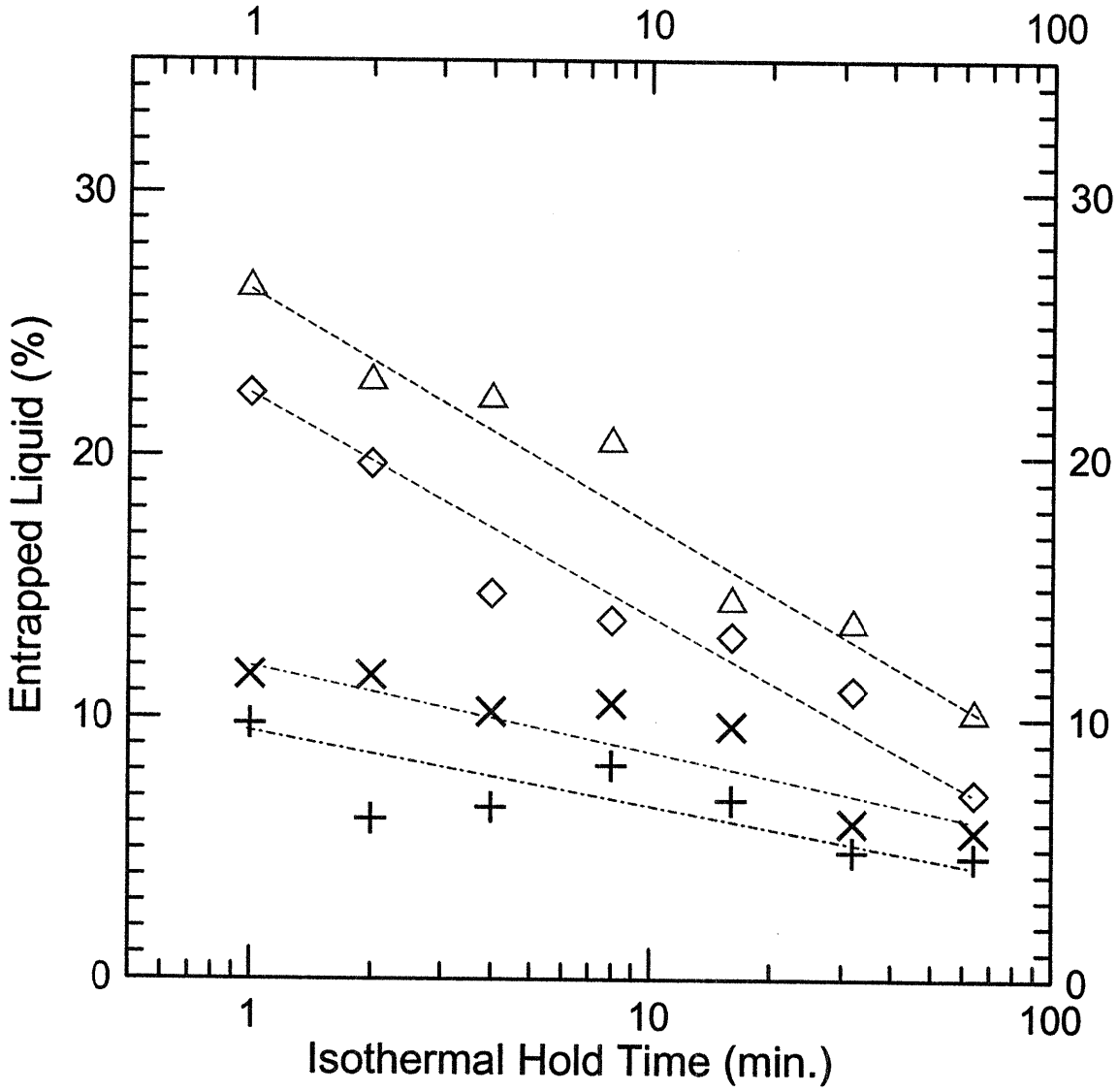

Figure 12: Evolution of entrapped liquid content as a function of material genealogy and isothermal hold time at 582°C.

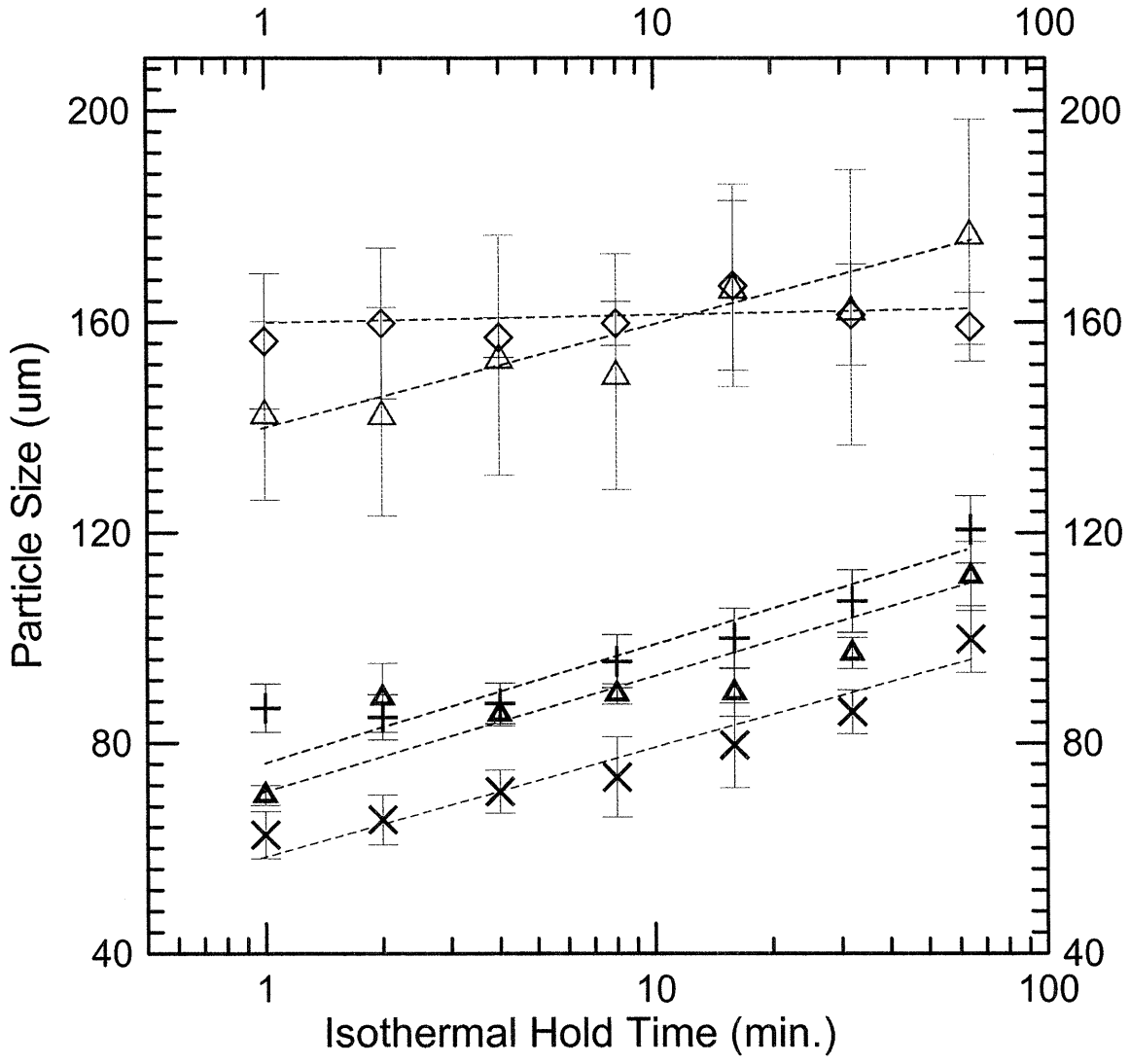

Figure 13: Evolution of particle size as a function of material genealogy and isothermal hold time at 582°C.

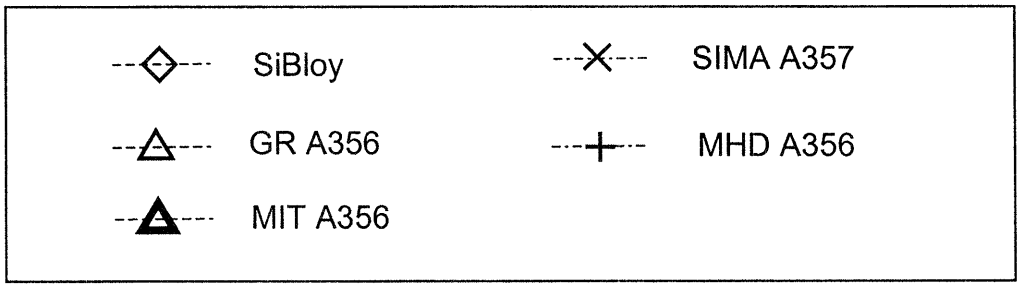

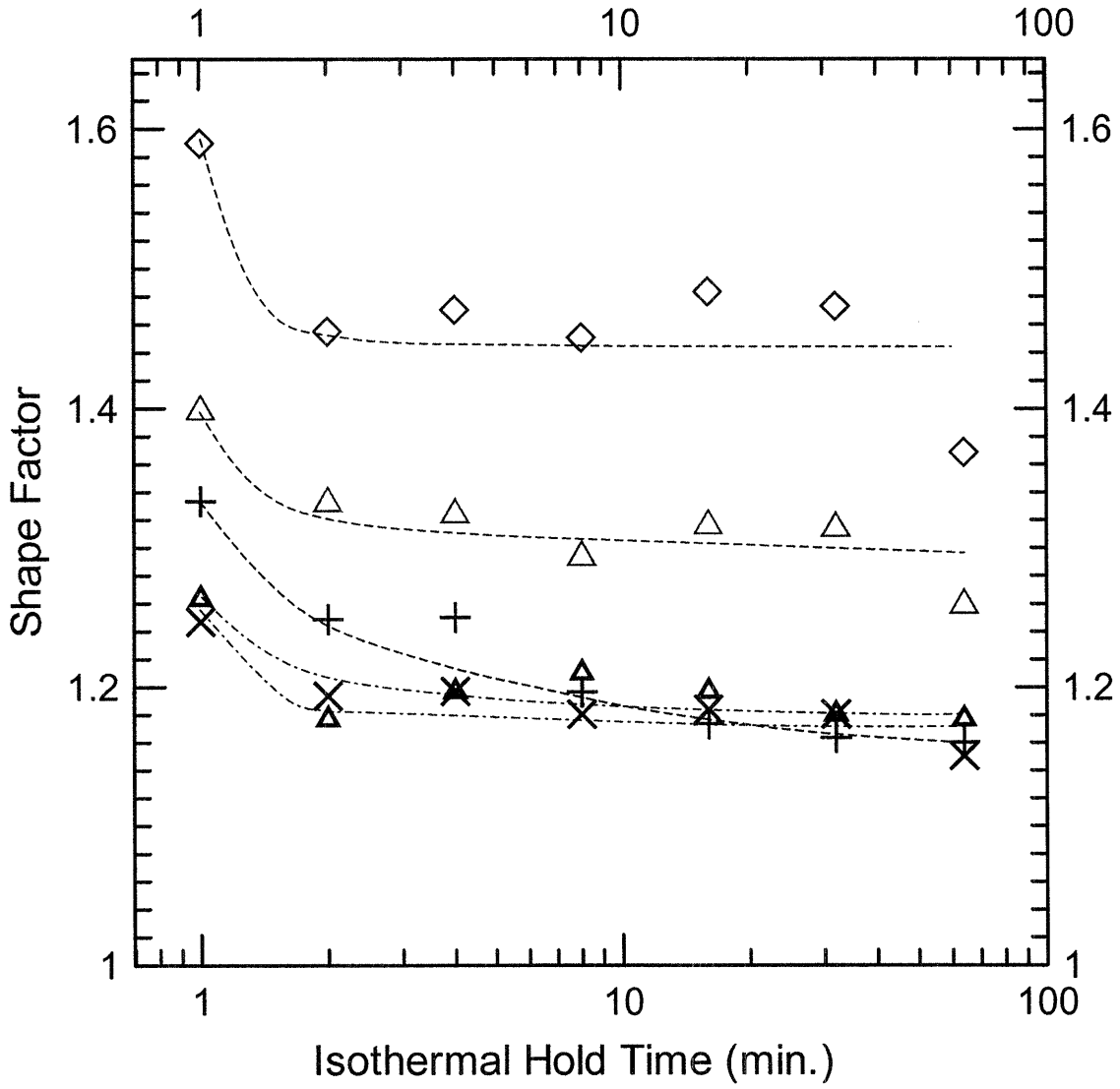

Figure 14: Evolution of shape factor as a function of material genealogy and isothermal hold time at 582°C.

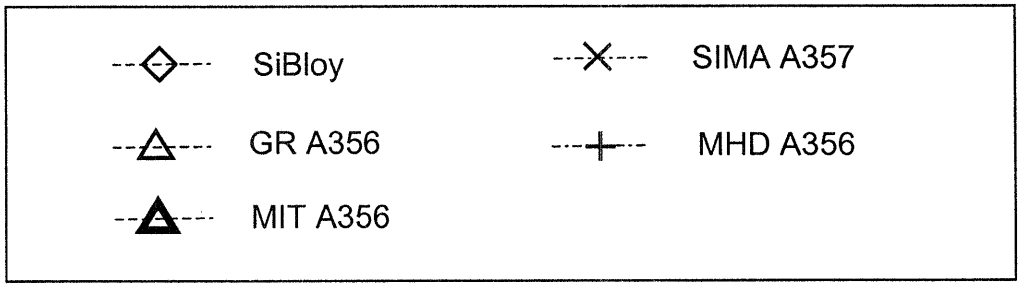

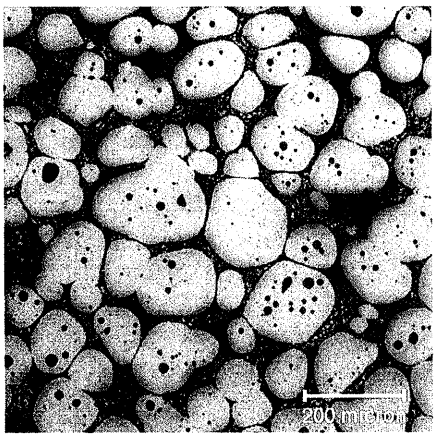

(a) MHD A356 at 578°C

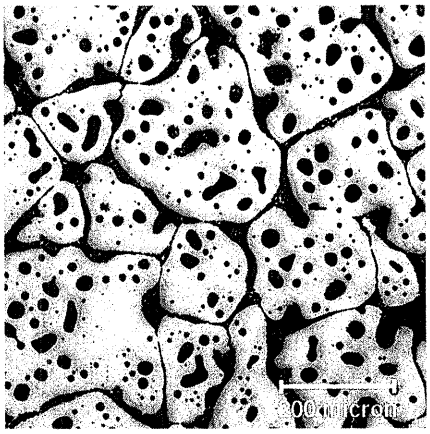

(b) GR A356 at 578°C

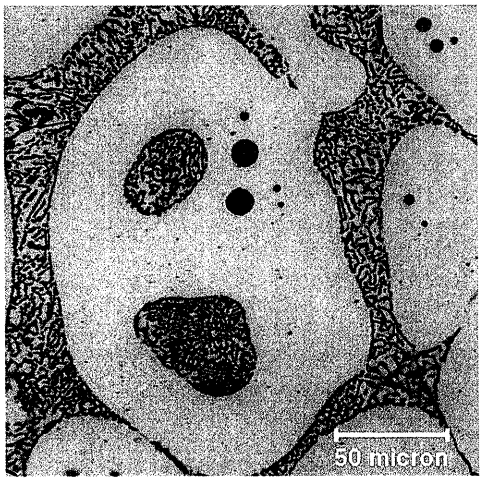

(C) Enlarged view of the entrapped liquid

Figure 15: Different morphologies of the entrapped liquid.

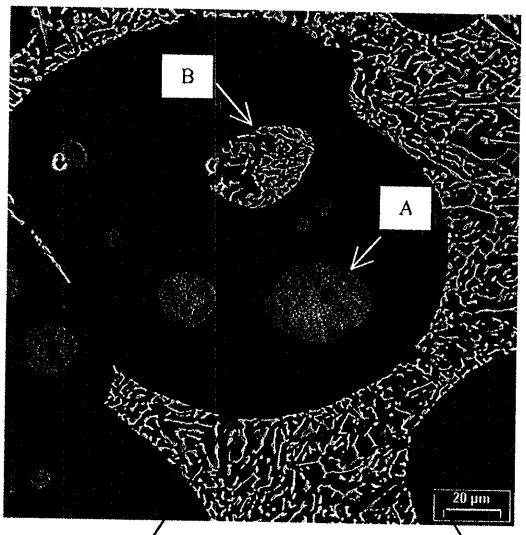

(a) GR A356 at 578°C, Keller's reagent

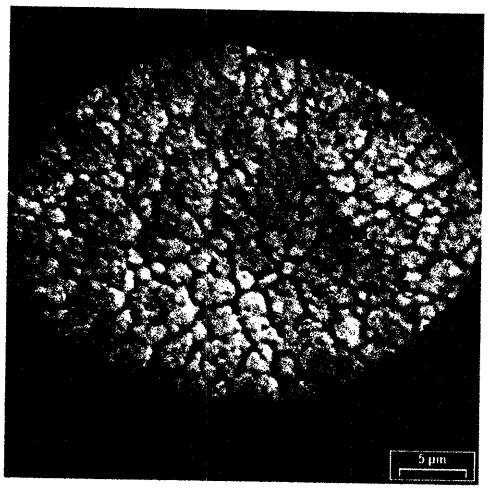

(b) Enlarged view of type A entrapped liquid, Keller's reagent.

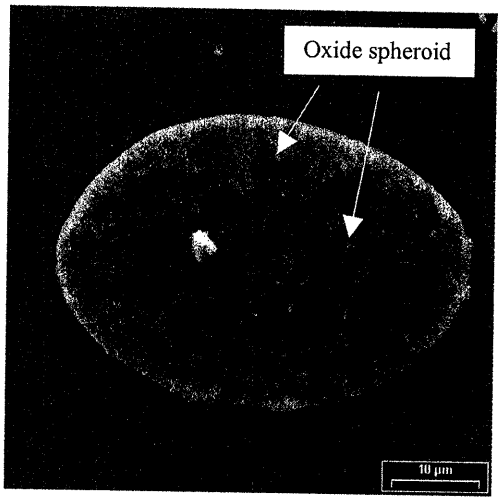

(c) Enlarged view of type A entrapped liquid, electropolishing.

Figure 16: SEM microstructure of the entrapped liquid, showing (a) two types of entrapped liquid in nature; (b) extremely fine eutectic grains, and (c) the nuclei-some oxide spheroids in each eutectic grain.